



Article

A Novel Polymerized Sulfur Concrete for Underground Hydrogen Storage in Lined Rock Caverns

Abdel-Mohsen O. Mohamed ^{1,*}  and Maisa El Gamal ² ¹ Uberbinder Limited, Littlemore, Oxford OX4 4GP, UK² Department of Environmental Sciences & Sustainability, College of Natural and Health Sciences, Zayed University, Abu Dhabi P.O. Box 144534, United Arab Emirates; maisa.elgamal@zu.ac.ae

* Correspondence: prof.mohsen.onsy@gmail.com

Abstract: Hydrogen is increasingly recognized as a viable solution to meet the growing global energy demand, making large-scale hydrogen storage essential for successfully realizing a full-scale hydrogen economy. Geological formations, such as depleted oil and gas reservoirs, salt caverns, and aquifers, have been identified as potential storage options. Additionally, unconventional methods like manufactured lined rock caverns and abandoned coal mines are gaining interest. This study introduces polymerized sulfur concrete (PSC) as a promising alternative to replace the current construction systems, which rely on Portland cement concrete and lining materials like stainless steel or polypropylene plastic liners. The paper presents the formulation of PSC, optimization of its compositional design, and evaluation of its physico-mechanical-chemical properties. The results demonstrate that PSC offers excellent mechanical strength, chemical resistance, and low permeability, making it highly suitable for underground hydrogen storage in lined rock caverns. The results showed that the manufactured PSC exhibits excellent physicochemical properties in terms of compressive strength (35–58 MPa), density (2.277–2.488 g/cm³), setting time (30–60 min), curing time (24 h), air content (4–8%), moisture absorption potential (0.17–0.3%), maximum volumetric shrinkage (1.69–2.0%), and maximum service temperature (85–90 °C). Moreover, the PSC is nonconductive and classified with zero flame spread classification and fuel contribution. In addition, the PSC was found to be durable in harsh environmental conditions involving pressure, humidity, and pH variations. It is also capable of resisting corrosive environments. In addition, the statistical modeling indicates that an overall mixture proportion of 32.5 wt.% polymerized sulfur, 32.5 wt.% dune sands, 17.5 wt.% LFS, and 17.5 wt.% GGBFS appear optimal for density values ranging from 2.43 to 2.44 g/cm³ and compressive strength ranging from 52.0 to 53.2 MPa, indicating that the PSC can sustain formation pressure up to about 5.3 km below the ground surface. Therefore, by addressing the critical limitations of traditional materials, PSC proves to be a durable, environmentally sustainable solution for lined rock caverns, reducing the risk of hydrogen leakage and ensuring the integrity of storage systems.

Keywords: polymerized sulfur concrete; physicochemical properties; hydrogen storage; lined rock caverns



Citation: Mohamed, A.-M.O.; El Gamal, M. A Novel Polymerized Sulfur Concrete for Underground Hydrogen Storage in Lined Rock Caverns. *Sustainability* **2024**, *16*, 8595. <https://doi.org/10.3390/su16198595>

Academic Editors: Jian Chen, Wen Zhang, Yongliang Liang and Muhammad Mamdouh Kabsha

Received: 8 September 2024

Revised: 27 September 2024

Accepted: 30 September 2024

Published: 3 October 2024



Copyright: © 2024 by the authors. Licensee MDPI, Basel, Switzerland. This article is an open access article distributed under the terms and conditions of the Creative Commons Attribution (CC BY) license (<https://creativecommons.org/licenses/by/4.0/>).

1. Introduction

Hydrogen is an element that has the potential to play a significant role in the energy transition towards a low-carbon economy. It can be produced from various sources, including natural gas, renewable electricity, biomass, and nuclear energy. Each source has advantages and disadvantages, and the choice of source will depend on factors such as availability, cost, and environmental impact. As the world transitions towards a low-carbon economy, hydrogen will likely play an increasingly important role in the energy mix.

In 2021, worldwide demand for hydrogen increased to 94.3 million metric tons per year (Figure 1; data from Statista Research Department [1]), consumed in the chemicals and refining sectors and still derived mainly from fossil fuels. However, the demand for

hydrogen is expected to grow significantly in the coming years (almost doubling by 2030) due to its potential use in other sectors, such as transportation, power generation, and heating [1]. For example, the transportation sector is one of the key sectors driving the growth in demand for hydrogen. Hydrogen-powered fuel cells are a promising alternative to fossil fuels in the transportation sector. Fuel cell electric vehicles (FCEVs) offer several advantages over battery-electric vehicles (BEVs), such as an extended range, faster refueling times, and higher energy density. The US accounts for about 50% of registered FCEVs, followed by Japan (about 25%), the European Union (11%, primarily in Germany and France), and Korea (8%) [2].

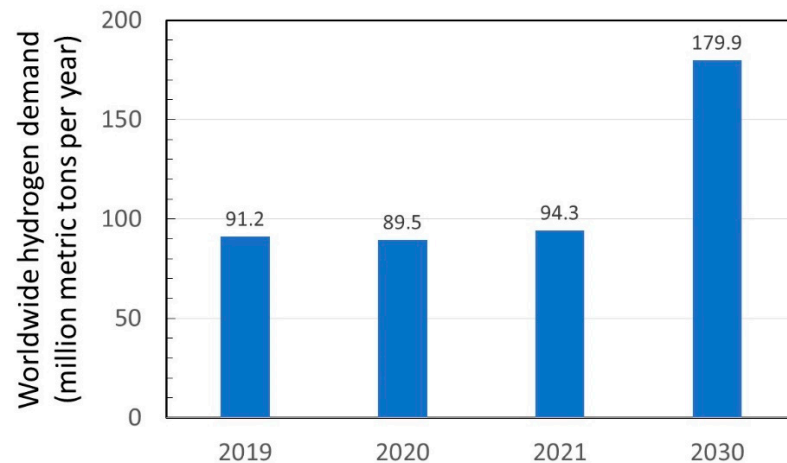


Figure 1. Annual global demand for hydrogen.

For the power generation and heating sector, when hydrogen is burned in a turbine or fuel cell, it produces electricity and heat with zero emissions. This makes it an attractive option for power generation and heating in sectors where emissions reduction is a crucial priority, such as the industrial and residential sectors. For example, the global building sector accounts for 30% of the global final energy use, nearly three-quarters of which is used for space heating, hot water production, and cooking [2]. Hydrogen can potentially contribute to the energy transition (e.g., through blending or methane production) and long-term strategies for de-carbonizing heat (e.g., pure hydrogen production from renewables). For example, in the UK, H21 North of England is the largest project, proposing to supply 100% hydrogen by pipeline to buildings (Northern Gas Networks, 2018). Also, in Europe, the ENE-FIELD demonstration was launched in 2012 and has installed more than 1000 small stationary fuel cell systems for residential and commercial buildings in 11 countries, with plans to increase the implementation to 2800 units [3]. In addition, in Japan, the ENE-FARM is a large-scale fuel cell demonstration and commercialization program aiming to install 5.3 million units by 2050 [4].

The industrial sector is another area that is driving the growth in demand for hydrogen. Hydrogen is a feedstock in various industrial processes, such as ammonia production, refineries, and steelmaking. In addition, hydrogen can be used as a feedstock to produce chemicals, such as methanol and ammonia. The demand for hydrogen for primary chemical production is expected to increase from 44 Mt/year (in 2019) to 57 Mt/year by 2030 as demand for ammonia and methanol grows [5]. For ammonia and methanol, the market is expected to increase for existing applications by 1.7% and 3.6% per year between 2018 and 2030, respectively [2]. Furthermore, the global demand for steel production from iron ore is expected to increase from its current market (4 MtH₂/year) by around 6% by 2030 [2]. For example, in the US, Air Products is developing a green hydrogen plant in Saudi Arabia that will be powered by 4 GW of renewable energy to produce hydrogen for the refining and chemical industries. In addition, the HYBRIT joint venture in Sweden was developed to explore the feasibility of hydrogen-based steelmaking using a modified DRI-EAF process design [6].

Large-scale storage methods (i.e., underground) are required to successfully enact a full-scale hydrogen economy. These methods can be characterized as (Figure 2): (i) conventional (i.e., depleted oil and gas fields, aquifers, and salt caverns) and (ii) unconventional (abundant coal mines and manmade lined/unlined rock cavern) [7–11]. They have several advantages [9,12,13]: (i) a significant storage capacity, as large volumes of hydrogen can be stored, hence meeting the full-scale hydrogen economy; (ii) a low environmental impact, reducing greenhouse gas emissions; and (iii) a safe and secure storage option for hydrogen.

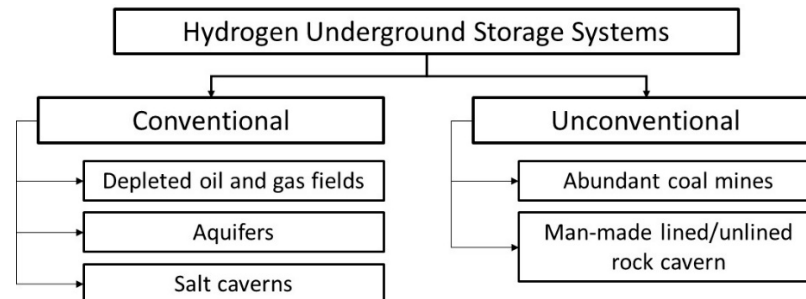


Figure 2. Hydrogen underground storage systems.

The number of underground hydrogen storage sites (UHSs) has grown over the last 100 years. Worldwide, a total of 642 UHSs were exploited until 2010 [8,14], distributed as 476 in depleted oil and gas fields, 82 in aquifers, and 76 in salt caverns (Figure 3a; data from Tarkowski [8]). They are distributed among regions/countries, most of the UHSs are located in North America (399 in the US, and 50 in Canada), whereas there are 130 UHSs in Europe, 50 in the Commonwealth of Independent States (CIS), 12 in Asia and Oceania, and 2 in South America (Figure 3b, data from Carnot-Gandolphe [15]).

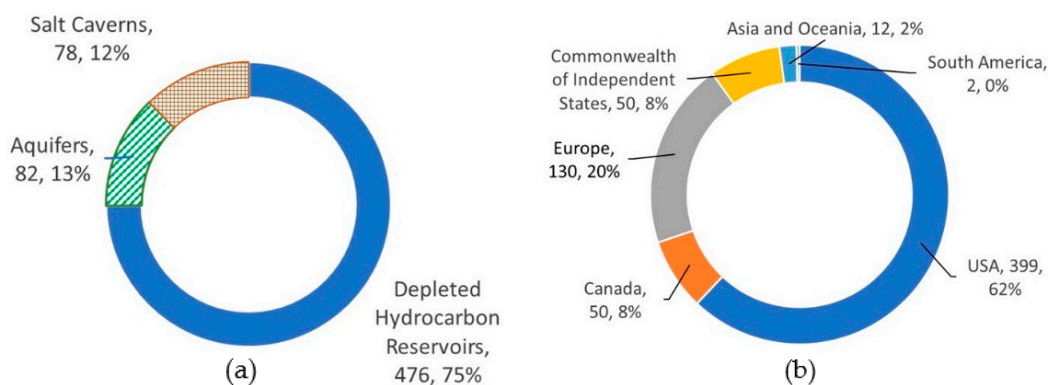


Figure 3. Worldwide share of underground hydrogen storage: (a) storage type and (b) storage region.

There are a number of technical issues associated with the conventional underground storage systems that impact their overall performance, such as the geological characteristics and the physico-chemical interactions of the host rock mass and the present pore fluid with the hydrogen gas. These issues are briefly discussed in Appendix A.

On the other hand, unconventional underground storage methods are currently being considered, such as abandoned coal mines and manmade lined/unlined hard rock caverns. In areas where the conventional methods and abandoned coal mines are not available, the use of manmade lined/unlined hard rock caverns, which are artificial chambers excavated (i.e., at shallow depths ranging from 400 m to 1200 m) in sedimentary deposits or bedded thin layers, can be implemented. Notably, the cavern storage systems have already been used to store natural gas in both unlined (Haje project, Czech Republic) and lined (Skallen project, Sweden) hard rocks ([16]), demonstrating their potential application for hydrogen storage. The advantages of these caverns are: (i) storing large amounts of gas that can

be withdrawn in multiple cycles and operate at low pressures [17]) and (ii) since the rock caverns are structurally stable, the amount of the cushion gas injected to maintain pressure within the storage system will be minimal.

During the operational lifespan of the cavern (i.e., cyclic injection and withdrawal of hydrogen), the cavern will experience complex mechanical, thermal, and hydraulic processes [18]. The cavern's stress state depends on depth, geological stress state, internal gas pressure, and injection/withdrawal rates [19]. It is also controlled by the cavern geometry [20], which influences stress redistribution during loading and unloading cycles [21]. Therefore, the cavern's complex system must accommodate the hydrofracturing (i.e., have a certain amount of ductility) [22]. It is also essential that the stress changes during the injection and withdrawal cycles do not cross the dilatancy boundary, which separates dilatancy behavior from compressibility behavior, resulting in increased permeability, reduced rock strength, and potential failure leading to loss of cavern integrity [23]. The gas temperature in the cavern fluctuates in response to thermodynamic and heat exchange processes, which are generally transmitted to the immediate vicinity of the cavern wall. Therefore, the cavern complex system must have an appropriate thermal expansion coefficient to accommodate the induced thermal stresses that affect the integrity of the cavern [24].

The current engineering practice of cavern design (Figure 4) is to encase the cavern with stainless steel or polypropylene plastic liners that function as an impervious layer, facilitating total containment of the stored hydrogen gas [16,25]). An ordinary Portland cement (OPC) concrete layer is placed to transfer the load from the cavern to the surrounding rock, providing a smooth surface for the steel or PVC liners [25]. Also, a groundwater drainage system is installed around the cavern's periphery to alleviate the hydrostatic pressure against the liner during depressurization [17].

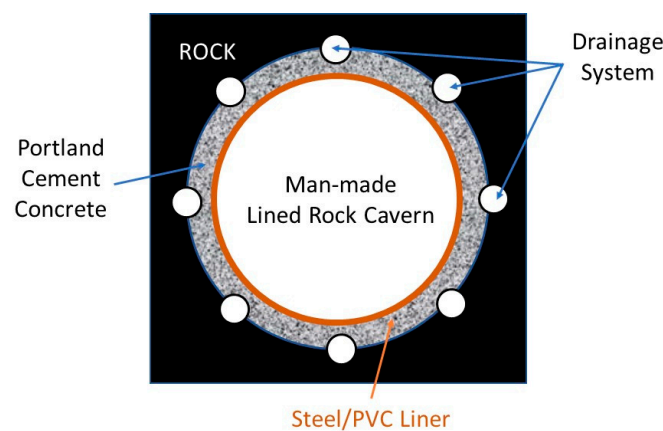


Figure 4. A schematic of a man-made lined rock cavern.

Notably, the lining system must possess the following characteristics [17,26]: (i) be gas-tight and chemically resistant to gas and to the possible condensates and impurities that it may contain; (ii) does not carry primary loads; (iii) be able to resist the stress and strain caused by the deformation of the cavern wall; (iv) can withstand the strain resulting from the fractures and cracks in the rock mass due to imposed gas pressure (i.e., cracks with openings of about 2 mm in the supported concrete layer are highly expected); (v) can withstand the maximum operating gas pressure; and (vi) be able to withstand the deformation due to cyclic loadings and chemical attacks.

In search of composite materials that are corrosion resistant, have high strength, low permeability, and moderate flexibility, and are fire resistant, polymerized sulfur concrete (PSC) has ascended to be the potential aspirant material. PSC is a material composed of polymerized sulfur, aggregate, and a curing agent [27–33]. Its unique properties make it a potential candidate for replacing OPC concrete in the underground hydrogen storage cavern design. A comparison between the properties of PSC and OPC concrete with

34.5 MPa strength is shown in Table 1 [27]. The PSC can be applied to (i) underground caverns: PSC can be used to line underground caverns, providing a durable and leak-resistant barrier for hydrogen storage; (ii) depleted oil and gas wells: these wells can be repurposed for hydrogen storage, with PSC used to seal and reinforce the wellbore; and (iii) underground tanks: PSC can be used to construct underground tanks for hydrogen storage.

Table 1. Polymerized fur concrete (PSC)'s properties compared with ordinary Portland cement (OPC) concrete (adopted from Mohamed and El Gamal [27]).

Property	Compared with OPC Concrete with 34.5 MPa Strength	Test Laboratory
Abrasion resistance	Much greater	Dow Chemical, Texas Division, Freeport, TX, USA
Bond strength to concrete	Much greater	Dow Chemical, Texas Division, Freeport, TX, USA
Bond strength to reinforcing steel	Greater	R. M. Hardy & Associates, Ottawa, ON, Canada
Coefficient of linear expansion	Equivalent	R. M. Hardy & Associates, Ottawa, ON, Canada
Compressive creep	Less	R. M. Hardy & Associates, Ottawa, ON, Canada
Compressive strength	Greater	EBA Engineering Consultants, Edmonton, AB, Canada; J. A. Smith & Associates, Nanaimo, BC, Canada; Bernard & Hoggan Engineering, Edmonton, AB, Canada
Corrosion resistance	Much greater	Sulfur Innovations, Calgary, AB, Canada; Mellon Institute, Pittsburgh, PA, USA
Durability under thermal cycling	Equivalent or higher	Ontario Research Foundation, Toronto, ON, Canada; Sulfur Innovations, Calgary, AB, Canada
Fatigue resistance	Much greater	Iowa State University, Ames, IA, USA
Fire resistance	Slightly less	Sulfur Innovations, Calgary, AB, Canada; Wamock Hersey, Vancouver, BC, Canada
Flexural strength	Greater	EBA Engineering Consultants, Edmonton, AB, Canada; J. A. Smith & Associates, Nanaimo, BC, Canada
Modulus of elasticity	Greater	R. M. Hardy & Associates, Ottawa, ON, Canada
Splitting tensile strength	Greater	R. M. Hardy & Associates, Ottawa, ON, Canada; J. A. Smith & Associates, Nanaimo, BC, Canada
Thermal conductivity	Less	Ontario Research Foundation, Toronto, ON, Canada
Water permeability	Much less	Chemical & Geological Laboratories, Calgary, AB, Canada

This study investigates the compositional control of a newly developed PSC and its mechanical and chemical behaviors under changing environmental conditions for its potential use as a corrosion-resistant material and as a healer to cracked rock in geological reservoirs for hydrogen storage in lined rock caverns (i.e., as a replacement to OPC concrete). In doing so, the PSC was manufactured using the following sustainable materials: (i) sulfur, a waste from the oil and gas industry, is polymerized using an organic polymer; (ii) dune sand from a sandy hump; (iii) ladle-furnace (LF) slag, waste from the electric arc furnace processes; and (iv) ground granulated blast furnace slag (GGBFS), waste from a cement factory. An experimental design approach was adopted, and a statistical method was employed to determine the optimal PSC ingredients. Several experiments were conducted to evaluate the physico-mechanical-chemical behaviors of the developed PSC. In addition, other previously reported PSC compositions were used to demonstrate the durability of PSC to chemical attacks, temperature changes, and an externally imposed vacuum pressure in an extreme environment.

2. Characterization of the Raw Materials

Selection and characterization of the raw materials is the first step in this study, as detailed in Figure 5.

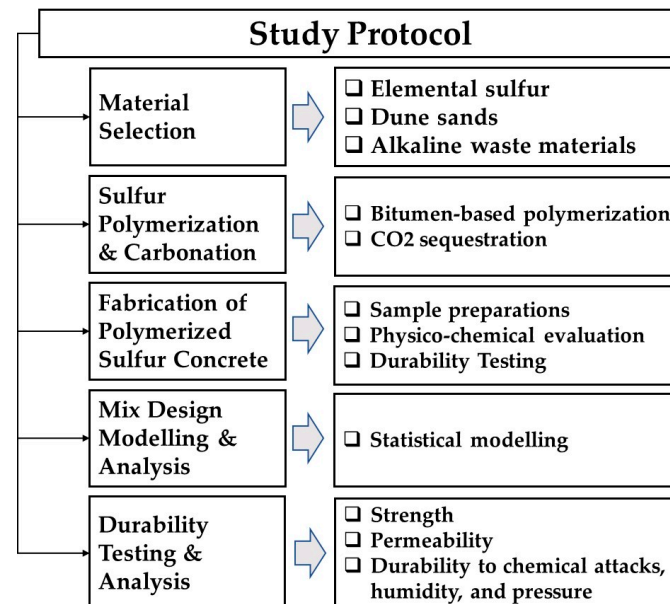


Figure 5. Study protocol.

2.1. Physical and Morphological Characteristics

Four feed materials for the PSC mixtures were collected locally from the United Arab Emirates (UAE). Granular elemental sulfur with a purity of 99.9% was obtained by ADNOC Sour Gas, Abu Dhabi, UAE, which was used to make the polymerized sulfur using the methodology presented in Mohamed and El Gamal [27]. Dune sand was collected from a sandy hump in the Al Ain area, UAE. Ladle-furnace slag (LFS) waste material, a byproduct from the electric arc furnace process, was collected from Emirates Steel Factory in Abu Dhabi, UAE. Finally, ground granulated blast furnace slag (GGBFS) was collected from the Al Sharjah Cement Factory, UAE. Additional information regarding these materials can be found in Mohamed et al. [32].

The granulometric distribution curves for the used aggregates are shown in Figure 6.

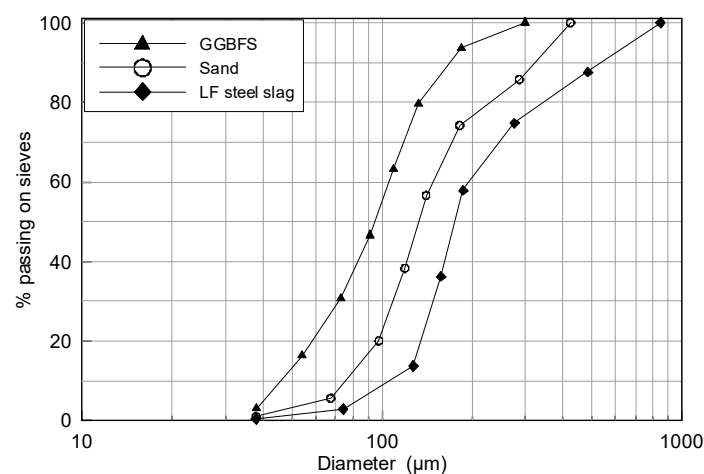


Figure 6. Grain size distributions of the used sand, LFS, and GGBFS.

The GGBFS is the finest aggregate (38 to 300 μm), followed by sand dune (38 to 400 μm) and LFS (38 to 850 μm). The graded materials belong to the fine aggregate size, as they include materials of mineral composition having particle sizes ranging from 38 to 850 μm .

The results shown in Table 2 indicate that the specific gravity of the GGBFS is slightly less than that of LFS and higher than that of sand. The specific surface area of GGBFS is higher than that of sand and LFS. The smaller the aggregate size, the greater its surface area. GGBFS has lower porosity and pore volume than LFS and sand.

Table 2. Specific gravity, surface area, and pore volume of the used aggregate materials.

Raw Materials	Sand	LFS	GGBFS
Specific gravity (g/cm^3)	1.69	3.30	2.86
BET surface area (m^2/g)	5.61	2.38	5.92
Langmuir surface area (m^2/g)	7.95	4.94	8.42
Micropore volume (cm^3/g)	1.71×10^{-3}	2.74×10^{-3}	3.41×10^{-4}
Total pore volume	5.22×10^{-3}	8.18×10^{-3}	3.04×10^{-3}

The scanning electron micrograph (SEM) images of the microstructure distributions of the used aggregates (Figure 7) indicate that (i) sand particles are smooth in texture and round in shape; (ii) LFS particles have a rough surface texture and include large numbers of micro-pores and internal pores; and (iii) GGBFS particles enclose smooth angular granules. Notably, the amount of sulfur required for the PSC highly depends on the particle size distribution and the maximum size of aggregates. Also, the amount of paste depends on the number of void spaces; LFS contains pores, which provide a durable adherence with polymerized sulfur. Therefore, the shape and porous structure of LFS make it necessary to use a high amount of polymerized sulfur when preparing the PSC.

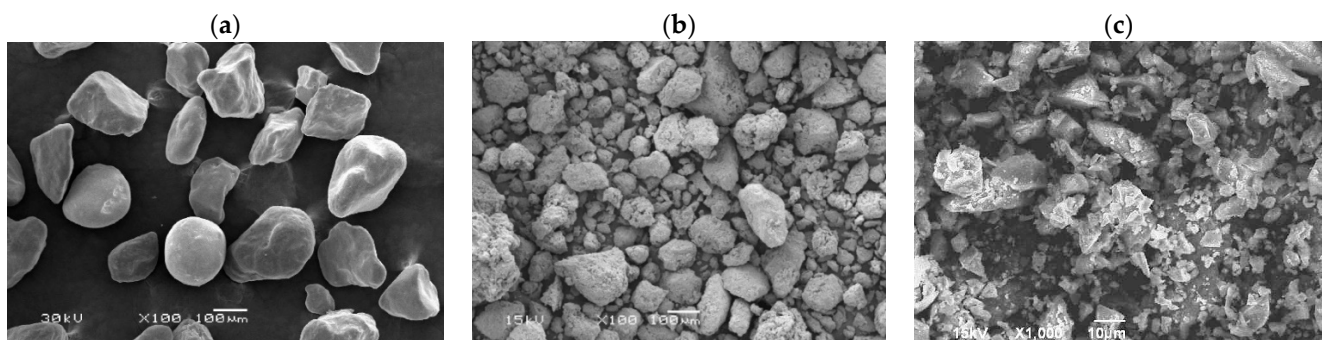


Figure 7. SEM images of the used materials: (a) sand, (b) LF slag, and (c) GGBFS.

2.2. Chemical and Mineralogical Characteristics

Determination of the chemical constituents of the aggregates and filler is essential to assess their mineralogical composition and to evaluate their adhesion properties. Table 3 shows the chemical compositions of the employed materials, mainly silicon, calcium, aluminum, magnesium, and iron oxides. The central oxide in sand is SiO_2 , whereas CaO is the central oxide in both LF steel slag and GGBFS. The CaO content of GGBFS was lower than that of LFS; however, its SiO_2 content was higher. The oxides MgO and Al_2O_3 were in significantly higher proportions in GGBFS compared with LFS.

Table 3. Chemical composition (weight %).

Component	Sand	LFS	GGBFS
SiO ₂	76.4	30.29	33.12
Fe (total)	0.68	3.42	0.48
Al ₂ O ₃	0.47	10.12	16.27
CaO	16.35	51.12	41.12
MgO	2.16	4.33	7.5
MnO	0.05	0.50	0.19
K ₂ O	1.13	0.03	0.36
Na ₂ O	2.10	0.01	0.07
Cr ₂ O ₃	0.02	0.05	0.01
Unidentified metal oxides	0.64	0.13	0.88
Sum	100	100	100
Loss on ignition (LOI)	6.01	1.4	2.34

The X-ray diffraction (XRD) analysis showed that the sand mainly comprises quartz mineral SiO₂, calcite CaCO₃, and dolomite CaMg(CO₃)₂. The LF steel slag is composed of Ca, Si, and Al oxides, wollastonite (β -CaO·SiO₂), anorthite CaO·Al₂O₃·2SiO₂, CaS, and α -Al₂O₃. The XRD analysis of GGBFS showed amorphous calcium aluminum silicate (AM) and larnite (calcium silicate) cemented by carbonates. The mineralogical analyses of each component showed the same composition as that revealed by the chemical analysis.

3. Sulfur Polymerization

Sulfur is thermoplastic; therefore, it can be melted and cooled back to a solid form. Because of this property, it can be mixed with aggregate or fillers to form sulfur-based concretes and composite materials that can be used as an alternative to conventional hydraulic OPC concretes. However, pure sulfur goes through an allotropic solid phase transition (upon cooling below 95.5 °C) from the monoclinic to the orthorhombic form, which is denser and occupies less volume [27]. Cooling of the sulfur results in an increase in density (shrinkage of the matrix), which introduces physical instabilities in the solid and makes the material highly stressed and susceptible to cracking and mechanical failure. To remedy the problem caused by sulfur's allotropic solid phase transition, elemental sulfur was modified by reacting with olefin hydrocarbon polymeric material (bitumen). As revealed in the SEM images shown in Figure 8a, the structure of elemental sulfur is composed of dense orthorhombic crystals of alpha form (S α).

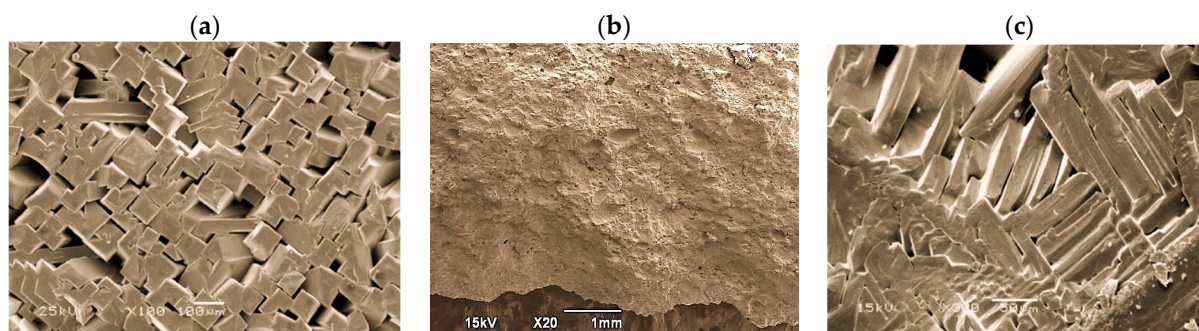


Figure 8. SEM images of (a) the crystalline morphology of pure elemental sulfur and (b,c) polymerized sulfur at different magnifications.

In comparison, polymerized sulfur consists of monoclinic plate-like microstructure crystals of beta form ($S\beta$) (Figure 8c) [27]. It is supposed that the growth of large crystals may be restricted because bitumen particles serve as nucleation sites that cause the formation of many small crystals instead of fewer large sulfur crystals. These plate-like microstructure crystals of micron size play a significant role in relieving the stresses produced from thermal expansion mismatch in concretes, helping to resist cracking, tolerating any thermal expansion, and developing minimal residual stresses and shrinkage upon cooling [27].

4. PSC Preparation and Characterization

The PSC was formulated from the polymerized sulfur, dune sand, LFS, and GGBFS, which are embedded in a matrix, whereby the polymerized sulfur fills the space between the aggregate's particles and glues them together. The mechanisms involved in the preparation of PSC are different from those used in the OPC concrete preparation. PSC is a thermoplastic material that is mixed and cast warm. On the solidification and cooling of the PSC to ambient temperature, the liquid polymerized sulfur binds the aggregate and forms a rigid PSC in minutes, reaching its maximum strength in less than 24 h. However, OPC concrete is prepared at ambient temperatures. It relies on the chemical hydration reactions during curing for at least 28 days to form the rigid OPC concrete and reach its maximum strength.

However, the aggregate's mineralogical properties and contents and the polymerized sulfur content determine the designed PSC's strength, workability, and durability. For example, dune sand is used to enhance the workability of the mixture because the particle is spherical and well-rounded, with a relatively smooth surface. The GGBFS is used because of its high surface area, which increases the bonding with the polymerized sulfur and the rough, angular shape of its crushed particles, reducing the high internal stresses during the cooling of the PSC mixture. Moreover, aggregates with an irregular geometry may reduce the workability of the mortar, but they enable the polymerized sulfur to adhere more easily to the surface of the grains (Gemelli et al. 2004). The molten polymerized sulfur acts as a binder material for the aggregates.

The PSC mixtures were prepared according to ACI 548.2R-93 [34], which involved mixing and placing the sulfur concrete. Since the mixing process is detailed in El Gamal et al. [35], only a brief description is given, as follows: the elemental sulfur was modified by mixing it with an organic material (natural bitumen at 2.5 wt.%) to form the polymerized sulfur. An emulsifying agent was used in that mixing process to enable uniform compatibility between elemental sulfur and the natural bitumen [27]. The reaction progress is tracked by visually observing the changes in viscosity and homogeneity of the studied mixture. The output product of this step is a sulfur-containing polymer (or polymerized sulfur) that has glass properties once it cools down. Secondly, aggregate materials were pre-heated to about 160 °C and mixed with the molten polymerized sulfur at 120–140 °C until a homogeneous mixture was obtained (ACI, 1993). Thirdly, the hot mixture was poured while still hot into pre-heated cylindrical and cubic molds and then settled on a table shaker for one minute. Finally, the casted samples were placed in an oven at 40 °C for 24 h for complete curing. The cured samples were kept and stored at room temperature for further testing, analysis, and characterization. The SEM examined the casted PSC and noted the presence of dark spots at the surface of the mixture due to the presence of the GGBFS particles.

The prepared PSC consisted of four ingredients: polymerized sulfur (referred to as X_1), dune sand (X_2), LFS (X_3), and GGBFS (X_4) with varying amounts as X_1 (0.3–0.4), X_2 (0.3–0.4), X_3 (0.15–0.25), and X_4 (0.15–0.20). The proportions of these ingredients were evaluated according to their mass fractions (e.g., 0.30 corresponds to 30% of the total mass of the mixture). The practical mass fractions of the ingredients are defined as the ones that achieve acceptable visual workability during mixing and casting. Therefore, preliminary mixes with different mass fractions were tried out, and the range of each ingredient was estimated.

The experimental results indicated that the PSC exhibited unique properties (Table 4). Depending on the mixture design, the recorded properties of the PSC after curing for 24 h

at 40 °C were: compressive strength ranging from 35 to 58 MPa, density from 2.277 to 2.488 g/cm³, air content from 4 to 8%, moisture absorption from 0.17 to 0.3%, and maximum volumetric shrinkage from 1.69 to 2.0%. In addition, PSC does not require curing and sets within 30–60 min. It is nonconductive with zero flame spread classification and zero fuel contribution. Moreover, the PSC maximum service temperature ranges from 85 to 90 °C, which is higher than that expected of a manufactured rock cavern for hydrogen storage.

Table 4. Physical properties of SPC after curing 24 h at 40 °C.

Property	Experimental Results
Compressive strength	35–58 MPa
Density	2.28–2.49 g/cm ³
Setting time	30–60 min
Curing time	24 h
Air content	4–8%
Moisture absorption	0.17–0.3%
Max. volumetric shrinkage	1.69–2.0%
Electrical conductivity	Nonconductive
Max. service temperature	85–90 °C
Flame spread classification	0
Fuel contribution	0

5. PSC Mixture Design Optimization

5.1. Modeling

In the mix design procedure, packing density, compressive strength, and stability are greatly influenced by the proportions of dune sand, LFS, GGBFS, and optimum proportions of polymerized sulfur. As the complexity of the experimental design increases, the ability to distinguish between main effects and interactions increases. The experimental design allows for (i) estimating the linear, the quadratic (i.e., linear and interaction terms), and the special cubic interaction effects of the components in the PSC mixture and (ii) comparing the models based on obtained responses (Table 5).

Table 5. Response regression model order.

Responses	Regression Model	Standard Deviation	R-Sq (%)	R-Sq (pred) (%)	R-Sq (adj) (%)	PRESS	p-Value
Density	Linear	0.04776	38.02	18.66	31.14	0.08085	0.004
	Quadratic	0.03085	79.88	51.22	71.26	0.04848	0.000
	Special cubic	0.01645	95.37	81.88	91.83	0.01801	0.000
Compressive Strength	Linear	5.42818	40.01	20.00	34.23	1075.19	0.002
	Quadratic	3.31535	82.83	60.73	75.47	527.865	0.000
	Special cubic	1.5456	96.98	89.04	94.67	147.341	0.000

The results shown in Table 5 indicate that the special cubic model provides an adequate fit to the PSC behavior (i.e., density and compressive strength), as in Equation (1).

$$Y = \varepsilon + \beta_1 X_1 + \beta_2 X_2 + \beta_3 X_3 + \beta_4 X_4 + \beta_{12} X_1 X_2 + \beta_{13} X_1 X_3 + \beta_{23} X_2 X_3 + \beta_{14} X_1 X_4 + \beta_{24} X_2 X_4 + \beta_{34} X_3 X_4 + \beta_{123} X_1 X_2 X_3 + \beta_{124} X_1 X_2 X_4 + \beta_{134} X_1 X_3 X_4 + \beta_{234} X_2 X_3 X_4 \quad (1)$$

where Y represents the response, the variable X₁ represents the polymerized sulfur, X₂ is the first aggregate (sand), X₃ is the second aggregate (LFS), and X₄ is the filler (GGBFS). For each

response, 14 coefficients were calculated, and the mixture design foresaw 26 experiments, that is, 13 different mixtures (Table 6).

Table 6. Proportions of PSC mixtures and measured responses.

Mixture ID	Input Ingredients Proportions				Output Experimentally Measured Responses (2 Responses for Each Mixture)	
	Polymerized Sulfur (X_1)	Sand(X_2)	LFS (X_3)	GGBFS (X_4)	Density(g/cm^3)(Y_1)	Compressive Strength (MPa) (Y_2)
1	0.30	0.30	0.25	0.15	2.37; 2.36	38.0; 39.5
2	0.30	0.30	0.20	0.20	2.49; 2.43	49.2; 48.0
3	0.30	0.40	0.15	0.15	2.29; 2.28	35.2; 36.0
4	0.40	0.30	0.15	0.15	2.32; 2.32	37.5; 39.5
5	0.35	0.30	0.15	0.20	2.30; 2.30	39.9; 41.0
6	0.30	0.35	0.15	0.20	2.31; 2.32	40.2; 42.0
7	0.325	0.325	0.175	0.175	2.43; 2.44	52.0; 53.2
8	0.3125	0.3125	0.2125	0.1625	2.38; 2.34	50.0; 53.6
9	0.3125	0.3125	0.1875	0.1875	2.44; 2.44	58.0; 54.0
10	0.3125	0.3625	0.1625	0.1625	2.38; 2.38	40.0; 38.4
11	0.3625	0.3125	0.1625	0.1625	2.31; 2.31	38.0; 39.0
12	0.3375	0.3125	0.1625	0.1875	2.41; 2.38	46.0; 48.0
13	0.3125	0.3375	0.1625	0.1875	2.44; 2.44	44.0; 42.0

Based on the obtained results (Table 7), regression equations were designed for the PSC for each response (i.e., density (Y_1) and compressive strength (Y_2)). Using a 5% significance level, a factor (i.e., X_1 or X_2 or X_3 or X_4) is considered to affect the response if the coefficients differ from zero significantly and the p -values < 0.050 (Morgan and Chemometrics 1991).

Table 7. Regression coefficients and the associated probability values (p -value) for each response.

Term	Density (Y_1)			Compressive Strength (Y_2)		
	Coefficient	T	p	Coefficient	T	p
X_1	200	-	-	36,485	-	-
X_2	131	-	-	25,674	-	-
X_3	367	-	-	76,581	-	-
X_4	285	-	-	24,074	-	-
X_1X_2	-657	-1.56	0.138	-134,154	-3.38	0.004
X_1X_3	-1361	-1.68	0.111	-301,855	-3.96	0.001
X_1X_4	-1105	-3.36	0.004	-108,576	-3.52	0.003
X_2X_3	-920	-1.21	0.241	-230,735	-3.24	0.005
X_2X_4	-800	-2.57	0.020	-43,941	-1.5	0.151
X_3X_4	-1338	-3.14	0.006	-185,071	-4.62	0.000

Table 7. Cont.

Term	Density (Y_1)			Compressive Strength (Y_2)		
	Coefficient	T	p	Coefficient	T	p
$X_1X_2X_3$	2416	0.98	0.342	748,447	3.23	0.005
$X_1X_2X_4$	2057	1.78	0.093	71,400	0.66	0.520
$X_1X_3X_4$	3302	3.41	0.003	508,563	5.59	0.000
$X_2X_3X_4$	1371	1.05	0.311	82,759	0.67	0.511

Figure 9 shows two normal probability plots, which are used to assess the normality of residuals in a model. The plot on the left corresponds to the “response is density” and the plot on the right corresponds to the “response is strength”. For the right plot (strength), the red data points follow the blue diagonal line fairly closely, indicating that the residuals for the strength response are approximately normally distributed. However, there is slight deviation at the tails, which might indicate some minor outliers or non-normality. Similarly, for the left plot (density), the red data points for the density response residuals also align closely with the diagonal line. There is a slight deviation from normality towards the ends, suggesting minor departures from a normal distribution. Both plots suggest an overall acceptable fit to the normal distribution, but there might be slight non-normality at the tails.

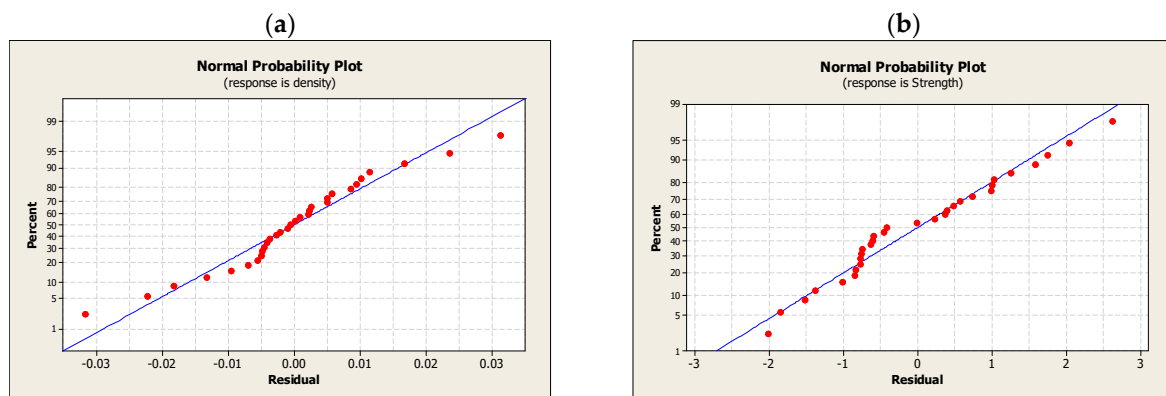


Figure 9. Normal probability plots of residual values for (a) density and (b) compressive strength of PSC.

5.2. Effect of Mixture Proportions on PSC Density

The experimental and statistical results indicated that PSC packing density (Y_1) was significantly affected by the mixture components' properties such as specific gravity, shape and sizes, total surface area, and void spaces. For example, considering the experimental results of mix designs 1 and 2, for constant PS (X_1) and sand (X_2) contents, as the content of the LFS (X_3) decreases and the GGBFS (X_4) increases, the solidified mixture density as well as the strength increases. Such an increase can be attributed to the specific mineralogical characteristics of the GGBFS (i.e., presence of amorphous calcium aluminate silicate and calcium silicate cemented by carbonates) leading to an increase in the densification, a high specific surface area that allows for more bonding with PS, less total pore volume within the GGBFS particles itself, and higher gradation and uniformity of particle sizes. In addition, the fact that GGBFS has a higher MgO content, leading to a higher catalytic reaction with the PS, the mixture bonding, density, and strength would be increased. Therefore, the contribution of the GGBFS to the overall design mix properties is highly important.

Moreover, to evaluate the impact of the PS content on the mix design properties, one uses mix designs 3 and 4, whereby the LFS (X_3) and GGBFS (X_4) are constants, the PS (X_1) content increased, and the sand (X_2) content decreased. In such a mixed design, the PS bonding with the LFS and GGBFS is enhanced, leading to a higher density and strength.

Therefore, the PS content significantly impacts the density and strength properties of the mix design.

It is worth noting that simple explanations of each component's role in a multi-component system would be difficult due to the interactions between the participating components. As seen below, the multi-component ($X_1X_3X_4$) significantly impacts the resulting mixture properties.

Positive coefficients (Table 7) for the three-blend mixtures $X_1X_3X_4$ (3302), $X_1X_2X_3$ (2416), $X_1X_2X_4$ (2057), and $X_2X_3X_4$ (1371) indicate that the three components act complementarily. That is, the mean acceptance score for the blend is more significant than that obtained by calculating the simple mean of the three acceptance scores for each mixture. The mixture $X_1X_3X_4$ is the three-blend mixture that might be considered significant ($T = 3.41$; $p = 0.003$). Negative coefficients for the two components, X_1X_2 , X_1X_3 , X_1X_4 , X_2X_3 , X_2X_4 , and X_3X_4 , indicate they are antagonistic. That is, the mean acceptance score is lower than that that can be obtained by calculating the simple mean of the two acceptance scores. Due to the relatively high specific gravity of steel slag (X_3), steel slag aggregate can be expected to yield a higher-density product than conventional mixes. The physical and chemical properties of aggregates at the micro-scale strongly impact the adhesive bond (strength and durability) between the polymerized sulfur and aggregates. These properties include surface-free energy, chemical interaction potential, and specific surface area. Mixes with higher polymerized sulfur contents have lower density.

The contour plots of the PSC mixtures for the density changes are shown in Figure 10, where one parameter remains constant each time. A contour plot is a graphical representation where contour lines connect points of equal value. In surface statistical modeling, contour plots often illustrate the relationship between the independent variables and one dependent variable. The dependent variable's values are represented by the contours (or "level curves"), making it easier to visualize how the variable changes over different combinations of the independent variables.

The main advantage of contour plots is their ability to reveal how sensitive a model is to changes in the input variables. By inspecting how rapidly or gradually contour lines shift, analysts can determine the sensitivity of the dependent variable to changes in independent variables, enabling more robust decision making.

The shape of the contour lines in a contour plot provides significant insights into the level of interaction between variables in a surface statistical model. Specifically, the way contour lines curve, intersect, or remain parallel can reveal whether the variables interact and, if so, the strength and nature of the interaction. Interpretations of the results based on contour shapes can be performed based on the following classification:

- (i) Straight and parallel lines: No or minimal interaction, meaning that the dependent variable is primarily influenced by one of the independent variables and the effect of the other variable is either constant or insignificant;
- (ii) Curved lines: Moderate to strong interaction, indicating non-linear relationships. This interaction means the effect of one variable on the dependent variable depends on the level of the other variable;
- (iii) Elliptical/circular lines: Moderate interaction, depending on the degree of elongation. A narrow ellipse suggests a stronger interaction, with the dependent variable being more sensitive to changes in both independent variables. In contrast, a more circular shape suggests a more balanced influence between the variables;
- (iv) Crossing or closely spaced lines: Strong interaction with possible critical points. This indicates that the dependent variable is extremely sensitive to changes in the combination of the independent variables. These crossings or abrupt changes in contour line density often mark critical points, such as maxima, minima, or saddle points, where the combination of both variables leads to significant changes in the response;
- (v) Twisted or S-shaped lines: Complex and non-linear interaction. This could suggest that the dependent variable's response to changes in the independent variables is not straightforward and that multiple regions of interaction exist, possibly indicating

non-linearities or multiple optimal points. Such contour patterns are common in systems with competing effects, where increasing one variable might initially improve the outcome but might later lead to a decrease, depending on the value of the second variable.

Figure 10 illustrates the contour plots for the density of the PSC, showing how the design space—the proportions of X_1 (polymerized sulfur), X_2 (sand), X_3 (LFS), and X_4 (GGBFS)—affects the density of the mixture. In the top-left plot, the design space is defined by X_1 , X_2 , and X_3 , with X_4 held constant. The highest density (2.294 g/cm^3) is found near the center, with closely spaced contour lines indicating high sensitivity to changes in LF slag (X_3). In the top-right plot, where X_1 , X_2 , and X_4 vary, the design space reveals that increasing X_4 (GGBFS) results in a density up to 2.355 g/cm^3 , with more gradual changes indicated by widely spaced contour lines. The bottom-left plot, which explores the design space of X_1 , X_3 , and X_4 , shows the highest density (2.416 g/cm^3) when both X_3 and X_4 are increased, with closely spaced contour lines signifying rapid changes in density. Finally, in the bottom-right plot, the design space consists of X_2 , X_3 , and X_4 ; balancing X_3 and X_4 leads to a density of 2.416 g/cm^3 , with strong interactions between LFS and GGBFS. In all plots, the proximity and shape of the contour lines indicate the sensitivity of the density to changes in the mixture components, with the closely spaced lines representing high sensitivity and the widely spaced lines indicating lower sensitivity. Notably, the highlighted heavy bold dotted lines represent the design spaces of the experimental density values that are used in the statistical modeling. These design spaces are crucial for determining the optimal mixture compositions to achieve the desired density outcomes, particularly in applications like underground hydrogen storage, where material density is critical.

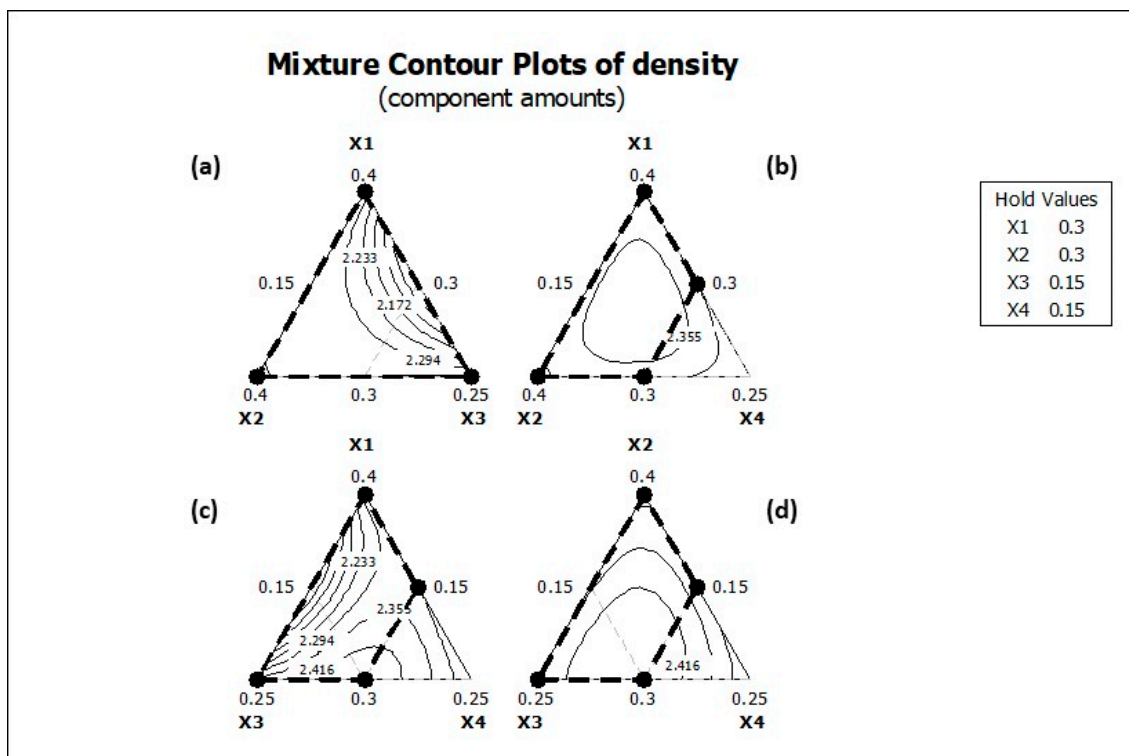


Figure 10. PSC mixtures contour plots for the density: (a) constant GGBFS (X_4) content at 0.15; (b) constant LF slag (X_3) content at 0.15; (c) constant sand (X_2) content at 0.3, and (d) constant polymerized sulfur (X_1) content at 0.3.

The PSC mixture response trace plot shown in Figure 11 is used to examine the effect of each component on the overall response. The plot discloses (i) the density changes when changing the proportion of each component while keeping all others in a constant

proportion and (ii) the effect of changing the corresponding component along an imaginary line connecting the reference blend to the vertex.

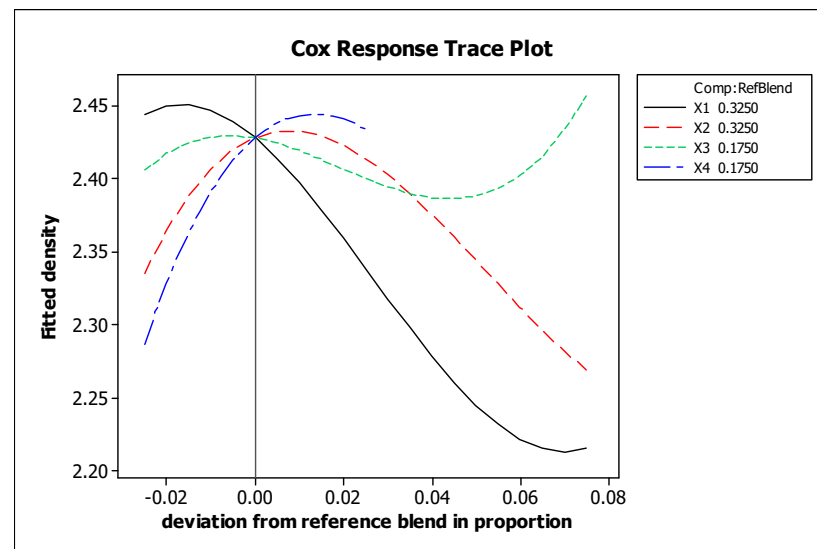


Figure 11. PSC mixtures response trace plot for density.

The results shown in Figure 11 indicate that (i) as the polymerized sulfur content (X_1) increases or decreases from the reference blend, the density decreases; (ii) as the sand content (X_2) increases or decreases from the reference blend, the density decreases; (iii) as the LF slag (X_3) increases from the reference blend, the density decreases, and as it decreases from the reference blend, the density almost remains constant and then decreases; and (iv) as the GGBFS (X_4) increases from the reference blend, the density increases, and as it decreases, the density decreases. Therefore, a slight increase in the GGBFS would impact the density, and then the density would decrease. Consequently, it can be stated that (i) the GGBFS has the highest impact on the density and (ii) the present overall mixture proportion (X_1 , X_2 , X_3 , and X_4 at 32.5, 32.5, 17.5, and 17.5%, respectively) seems to be suitable for an optimal density of 2.43–2.44 g/cm³.

5.3. Effect of Mixture Proportions on PSC Compressive Strength

Compressive strength is known to be a function of the density of PSC, and an increase in density results in higher compressive strength. Bonding between aggregate and polymerized sulfur is an essential factor for PSC strength. Bonding is due, in part, to the interlocking of the aggregate and the hardened polymerized sulfur due to the roughness of the surface of the former. A rougher surface, such as that of crushed particles, results in a better bond due to mechanical interlocking; a better bond is also usually obtained with mineralogically heterogeneous particles. In addition, the bond is affected by other physical and chemical properties of the aggregates.

With this design, polymerized sulfur in a small amount is required to fill the voids in the aggregate mixture. It was established that a larger polymerized sulfur/aggregate ratio tends to decrease the compressive strength of the formed PSC due to the thick layer of polymerized sulfur around the aggregate particles, which leads to brittle products. In addition, the polymerized sulfur ratio significantly influenced the mixture's rheological properties, reflected in the resulting PSC's compatibility, density, and void content. In lower polymerized sulfur/aggregate ratio cases, the molten mixture became excessively dry and thick, preventing adequate distribution of the materials and significantly reducing the formed PSC's compressive strength. An aggregate grading yielding maximum solid density and particle interlock is highly desirable for SPC [27]. Maximum particle interlocking leads to high strength, whereas minimum voids in a specific material composition are conducive to high strength and low compression. This coincides with the correlation

between mechanical strength and porosity since strength is dependent on the concrete microstructure and porosity is related to the movement of chemical substances into and out of the concrete, consequently affecting its durability.

The results indicated that the compressive strength (Y_2) of PSC was significantly affected by the mixture components. Positive coefficients (Table 7) for the three-blend mixtures, $X_2X_3X_4$ (82,759), $X_1X_2X_3$ (748,447), $X_1X_2X_4$ (71,400), and $X_1X_3X_4$ (508,563), indicate that the three components act complementarily. That is, the mean acceptance score for the blend is more significant than that obtained by calculating the simple mean of the three acceptance scores for each mixture. The mixtures $X_1X_2X_3$ ($T = 3.23$; $p = 0.005$) and $X_1X_3X_4$ ($T = 5.59$; $p = 0.000$) are the three-blend mixtures that might be judged as significant. Negative coefficients for the two components, X_1X_2 , X_1X_3 , X_1X_4 , X_2X_3 , X_2X_4 , and X_3X_4 , indicate they are antagonistic. That is, the mean acceptance score is lower than that obtained by calculating the simple mean of the two acceptance scores. All the two components are significant except X_2X_4 , which has a high p -value. Based on the linear coefficients of the four ingredients (X_3 (76,581), X_1 (36,485), X_2 (25,674), and X_4 (24,074)), it seems that LF slag is the main driver for the compressive strength developments.

The PSC contour plots of the compressive strength are shown in Figure 12, where one parameter remains constant each time. Figure 12 presents the contour plots for the compressive strength of the PSC, highlighting how the design space—the proportions of X_1 (polymerized sulfur), X_2 (sand), X_3 (LFS), and X_4 (GGBFS)—affects the compressive strength of the mixture. In the top-left plot, the design space consists of X_1 , X_2 , and X_3 , with X_4 held constant. The highest compressive strength (60 MPa) is observed in the center of the plot, with closely spaced contour lines indicating high sensitivity to changes in these components, especially LFS (X_3). In the top-right plot, where X_1 , X_2 , and X_4 vary, the design space shows that increasing X_4 (GGBFS) leads to a compressive strength of up to 50 MPa, with more gradual changes indicated by the widely spaced contour lines. The bottom-left plot, which explores the design space of X_1 , X_3 , and X_4 , shows the highest compressive strength (70 MPa) when both X_3 and X_4 are increased, with closely spaced contour lines indicating rapid changes in strength. In the bottom-right plot, where X_2 , X_3 , and X_4 vary, the compressive strength reaches 70 MPa, with a strong interaction between LFS (X_3) and GGBFS (X_4). In all plots, the proximity and shape of the contour lines reflect the sensitivity of the compressive strength to changes in the mixture components. Closely spaced lines indicate high sensitivity, while widely spaced lines suggest a more gradual response. Notably, the highlighted heavy bold dotted lines represent the design spaces of the experimental strength values that are used in the statistical modeling. These design spaces are essential for identifying optimal mixture compositions to achieve the desired compressive strength, particularly for applications requiring high structural integrity, such as PSC materials.

The PSC mixture response trace plot (Figure 13) is used to examine the effect of each component on the overall response. The plot reveals how the compressive strength changes when changing each component's proportion while keeping all others in a constant proportion. The plot discloses (i) as the sulfur content (X_1) increases or decreases from the reference blend, the compressive strength decreases; (ii) as the sand content (X_2) increases or decreases from the reference blend, the compressive strength decreases; (iii) as the LF slag (X_3) increases from the reference blend, the compressive strength increases up to a specific increase in its content, and as it decreases from the reference blend, the compressive strength decreases sharply; and (iv) as the GGBFS (X_4) increases from the reference blend, the compressive strength increases, and as it decreases, the compressive strength increases.

Therefore, the slight increase in both LF slag and GGBFS would increase the compressive strength, then the density would be decreased. However, a slight rise in LF slag and a slight decrease in the GGBFS would contribute to increased compressive strength. The existing overall mixture proportions (X_1 , X_2 , X_3 , and X_4) of 32.5, 32.5, 17.5, and 17.5%, respectively, appear to be optimal for compressive strength values ranging from 52.0 to

53.2 MPa, indicating that the PSC is capable of sustaining a formation pressure up to about 5.3 km below the ground surface.

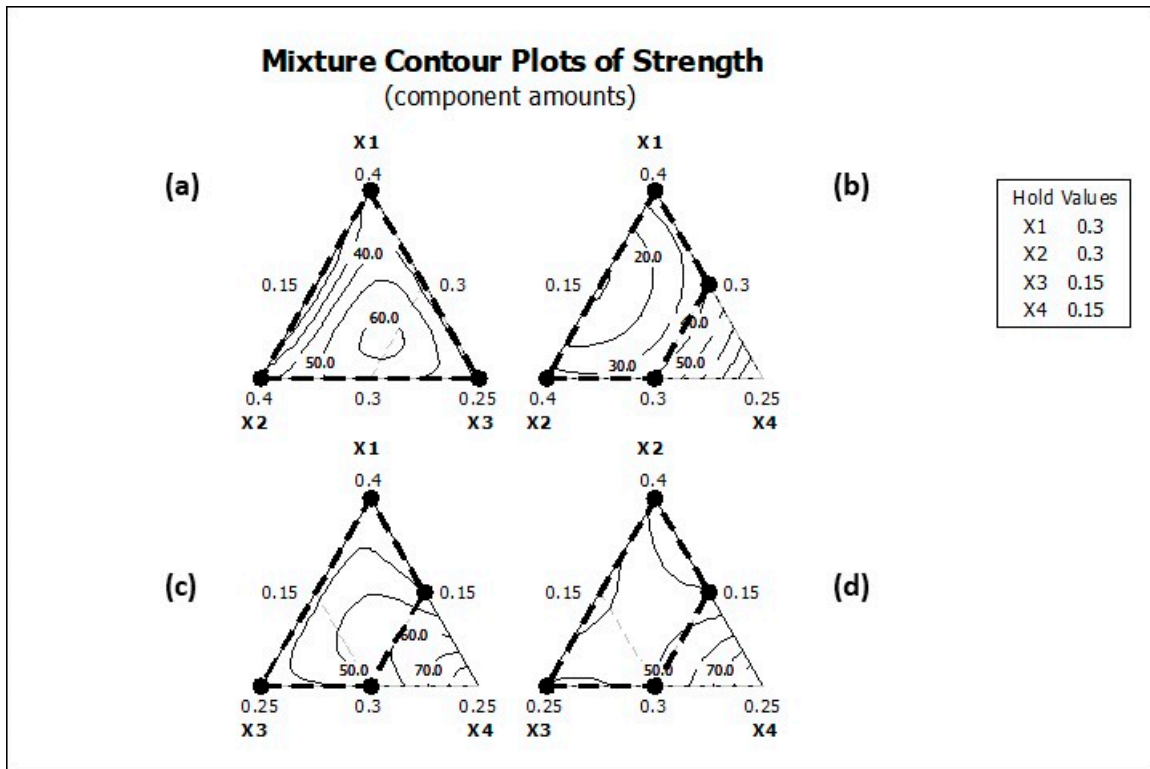


Figure 12. PSC mixture contour plots for the compressive strength: (a) constant GGBFS (X_4) content at 0.15; (b) constant LF slag (X_3) content at 0.15; (c) constant sand (X_2) content at 0.3, and (d) constant polymerized sulfur (X_1) content at 0.3.

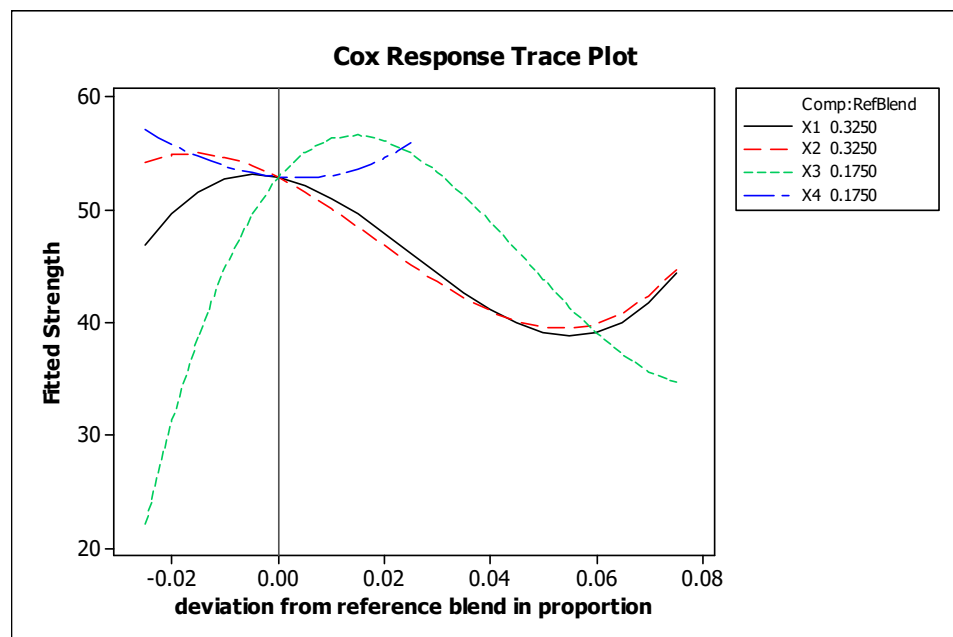


Figure 13. PSC mixtures response trace plot for compressive strength.

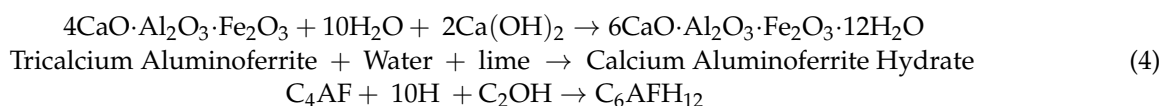
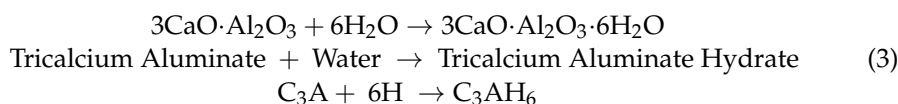
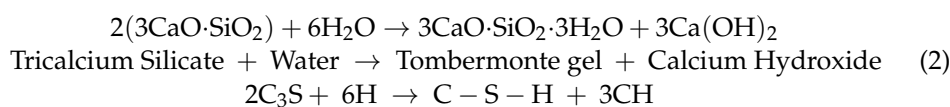
6. Durability

Figure 14 shows the compressive strength reduction of a PSC mixture consisting of 21% polymerized sulfur, 38% crushed sand, 24% dune sand, 8% carbonated LF slag, and 9% carbonated GGBFS after exposure for 18 months to different environmental conditions [32]: (i) water at room temperature (23 ± 3 °C); (ii) water at 60 °C; (iii) 20% sulfuric acid solution; and (iv) 5% sodium chloride solution.

These results indicated that the PSC manufactured with carbonated alkaline solid wastes has a high tolerance to both acidic and saline environments because uncarbonated alkaline solid wastes generally tend to expand due to the presence of free lime [fCaO] and free magnesium oxide [fMgO] [32]. The expansion of fCaO and fMgO, as well as the conversion of di-calcium-silicate [C₂S] and the oxidation of iron and carbonation of CaO and MgO, results in volumetric instability (swelling). Notably, lime [CaO] can be thoroughly hydrated in a few days when immersed in water; MgO hydrates much slower, causing significant volume changes for months or years. To decrease the volume instability caused by the swelling components, treatment techniques, such as using additives, steam treatment, open-air stockpiling (aging), and mineral carbonation, are employed.

Minimum compressive strength reduction was observed when the PSC was exposed to distilled water at room temperature. However, as the temperature increases, the strength reduction increases. The strength reduction could be attributed to many factors:

- a. **Formation of New Minerals:** Considering the elemental analysis of the sand, LFS, and GGBFS (Table 5), there are considerable amounts of metal oxides that have an essential role when they contact water at variable temperatures. The availability of these types of oxides could lead to the formation of tri-calcium silicate (CaO·SiO₂), tri-calcium aluminate (CaO·Al₂O₃), and tetra-calcium almino-ferite (CaO·Al₂O₃·Fe₂O₃). With water availability, the following reactions will take place:



and new minerals or cementing agents such as calcium silica hydrate (CSH), tri-calcium aluminate hydrate (C₃AH₆), and calcium almino-ferrite hydrate (C₆AFH₁₂) are formed. The percentage of formed minerals is shown in Table 8 (data from Mohamed and El Gamal [27]). However, these newly developed minerals may deposit in the pores without polymerized sulfur binding, reducing strength.

- b. **Discontinuity of the Pores:** As per Mohamed and El Gamal [27], the SEM analysis of the PSC samples immersed in heated deionized water at 60 °C showed small and discontinuous voids. These voids serve as stress relief sites and improve the material's durability. Also, voids reduce the polymerized sulfur required to coat the mineral aggregate, minimizing the shrinkage.
- c. **Pore Diameter:** Based on void size evaluation from the results of the SEM using image analysis software, the diameter Feret ratio increases as temperature increases, indicating that the voids' sizes increased [27];
- d. **Atomic Sulfur Content:** As per the EDX analysis [27], the percentage of atomic sulfur in the PSC decreased by 4.4% due to heating at 60 °C, which is compatible with the presence of voids in PSC at elevated temperatures as per the SEM results. However,

based on the gravimetric analysis, no loss in elemental sulfur was noted at 60 °C [27], indicating no formation of sulfur gas and possible formation of metal sulfide forms.

Table 8. Percentage formed mineral compositions with time.

Mineral Type	Curing Time		
	1 Day	2 Days	7 Days
Sulfur	27.9–35.4	28.0–35.2	28.4–31.5
Quartz (SiO ₂)	44.0–56.2	42.7–50.0	44.0–50.5
Aluminium oxide hydrate (5Al ₂ O ₃ nH ₂ O)	2.9–6.1	4.4–7.0	1.7–7.9
Calcite (CaCO ₃)	2.2–2.9	2.5–5.0	2.0–3.8
Calcium silicate hydrate (Ca _{1.5} SiO _{3.5} nH ₂ O)	2.3–4.4	3.7–4.8	1.8–5.0
Plagioclase (CaAlSi ₃ O ₈)	3.9–7.5	3.2–3.6	2.5–4.7
Hematite (Fe ₂ O ₃)	1.1–3.5	1.0–2.5	2.2–2.5
Dolomite (CaMg(CO ₃) ₂)	1.0–1.4	1.0	1.5–3.9
Calcium aluminum oxide hydrate (Ca ₃ Al ₂ O ₆ nH ₂ O)	0.0–1.9	1.0–1.3	0.0–1.2

About a 3% reduction in strength was observed when samples were exposed to an acidic environment for six months; however, no further decrease was observed beyond this period. This behavior can be explained by evaluating the possible interaction between the PSC and the 20% sulfuric acid solution. Sulfuric acid is a strong mineral acid that can aggressively react with composite components. The reaction mechanisms depend on the chemical properties of each material. For polymerized sulfur, sulfuric acid might have a minimal effect on polymerized sulfur due to sulfur's intrinsic resistance to acidic environments. However, any residual bitumen within the polymerized sulfur matrix could be vulnerable to degradation, possibly leading to softening or surface erosion. For sand, silicon dioxide is generally resistant to sulfuric acid at ambient temperatures, but impurities within the sand, such as calcium or magnesium compounds, could react to form soluble sulfates. For LFS, since it contains high amounts of calcium and aluminum oxides that can react with sulfuric acid to form calcium sulfate (gypsum) and aluminum sulfate, these reactions may weaken the composite's structural integrity over time: (a) $\text{CaO} + \text{H}_2\text{SO}_4 \rightarrow \text{CaSO}_4 + \text{H}_2\text{O}$ and (b) $\text{Al}_2\text{O}_3 + 3\text{H}_2\text{SO}_4 \rightarrow \text{Al}_2(\text{SO}_4)_3 + 3\text{H}_2\text{O}$. The formation of gypsum could lead to expansion and cracking, compromising the material's mechanical properties. Finally, the GGBFS, in the presence of sulfuric acid, can undergo a reaction similar to LFS, where calcium silicate reacts to form gypsum, potentially reducing the material's strength. The glassy phase of GGBFS may dissolve slowly, leading to the leaching of calcium and silica: $\text{Ca}_2\text{SiO}_4 + \text{H}_2\text{SO}_4 \rightarrow \text{CaSO}_4 + \text{SiO}_2(\text{gel}) + \text{H}_2\text{O}$. However, prolonged exposure can reduce the composite's durability in acidic environments.

The observed plateau after six months can be explained in view of a study by Mohamed and El Gamal [27], where PSC was tested with variable pH values (pH4 to pH9), and the results showed that a plateau was reached at about 75 days for the leachability of sulfur, Ca, Mg, Al, and Fe. Sulfur leachability was independent of pH, while other metals' leachability was pH dependent. This means that the PSC was stable after 75 days.

Similar behavior was observed when specimens were subjected to a saline environment. This behavior can be explained by evaluating the possible interaction between the PSC and the 5% sodium chloride solution. Sodium chloride solutions can promote chloride-induced corrosion, especially in environments exposed to fluctuating moisture conditions. The interaction mechanisms of each component with NaCl are highlighted below. Polymerized sulfur is generally inert to sodium chloride, as neither sulfur nor bitumen is susceptible to chloride-induced corrosion under ambient conditions. SiO₂ is chemically stable for sand in the presence of sodium chloride, with little to no reaction. However, chloride ions could promote the dissolution of trace impurities, such as iron or

calcium oxides. LFS contains calcium oxides, which can react with chloride ions to form soluble calcium chloride: $\text{CaO} + 2\text{NaCl} + \text{H}_2\text{O} \rightarrow \text{CaCl}_2 + 2\text{NaOH}$. This reaction can lead to leaching, which reduces the binding capacity of the slag, potentially affecting the overall durability of the composite. Finally, the GGBFS may be susceptible to chloride attack in the presence of moisture. Chloride ions can penetrate the composite, reacting with calcium silicates and forming calcium chloride. Over time, this can lead to the de-passivation of any embedded metals and the subsequent initiation of corrosion processes: $\text{Ca}_2\text{SiO}_4 + 2\text{NaCl} + \text{H}_2\text{O} \rightarrow \text{CaCl}_2 + \text{Na}_2\text{SiO}_3$. While polymerized sulfur and sand may resist chloride ions, the interaction of LFS and GGBFS with NaCl can weaken the material's structural integrity.

Therefore, PSC shows variable resistance to chemical agents. In a 20% sulfuric acid environment, reactions with LFS and GGBFS can produce soluble sulfates such as gypsum, which may degrade the material over time. The polymerized sulfur matrix is relatively stable, but acid exposure can weaken the composite due to slag reactions.

In a 5% NaCl solution, the composite remains stable in the short term, particularly the polymerized sulfur and sand. However, the chloride-induced degradation of LFS and GGBFS can lead to calcium leaching, leading to the material gradually losing strength and increasing its susceptibility to corrosion.

Both environments suggest that while polymerized sulfur adds chemical resistance, the presence of LFS and GGBFS can significantly impact the long-term durability of the composite under aggressive conditions.

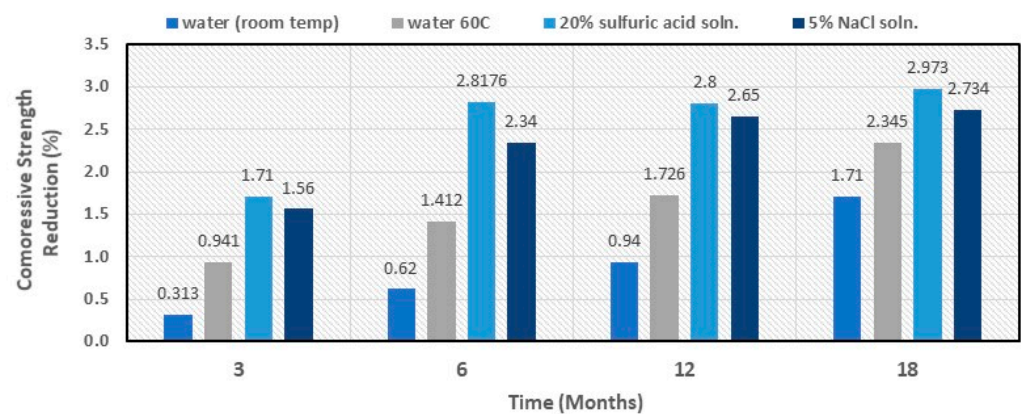


Figure 14. Compressive strength reduction of PSC after 18 months of exposure to variable chemical and temperature environments.

However, it was not as high as that for the acidic condition due to the possible formation of high-swelling mineral products such as ettringite and thaumasite [29], which are valuable minerals in mitigating the potential cracks in the rock mass. The ettringite and thaumasite formation mechanisms and PSC durability enhancements due to carbonation and sulfur polymerization can be highlighted as follows.

As discussed, LFS and GGBFS are highly alkaline materials containing a range of oxides, including calcium oxide (CaO), alumina (Al_2O_3), silica (SiO_2), smaller amounts of magnesium oxide (MgO) and iron oxides (FeO), and a high glass content that imparts latent hydraulic properties. When these materials are exposed to water, a range of hydration reactions occur, potentially resulting in the formation of various cementitious compounds and secondary minerals such as ettringite, a hydrated calcium sulfoaluminate mineral ($\text{Ca}_6\text{Al}_2(\text{SO}_4)_3(\text{OH})_{12} \cdot 26\text{H}_2\text{O}$), and thaumasite ($\text{CaSiO}_3 \cdot \text{CaCO}_3 \cdot \text{CaSO}_4 \cdot 15\text{H}_2\text{O}$). Ettringite formation can be influenced by alumina availability, sulfur content, and high pH levels [29]. Ettringite formation occurs early in the hydration process but may continue to develop over time. While ettringite contributes to initial strength development, its expansion under certain conditions (e.g., moisture and temperature changes) can lead to cracking and deterioration of materials.

However, thaumasite ($\text{CaSiO}_3 \cdot \text{CaCO}_3 \cdot \text{CaSO}_4 \cdot 15\text{H}_2\text{O}$) is a mineral that forms under specific conditions involving the presence of carbonates, sulfates, and silicates in an environment with high moisture and low temperatures (often below 15°C). Its formation requires silicate and sulfate sources, as well as low temperatures and humidity. Its formation is slower than ettringite, but when present, it can significantly deteriorate materials by disrupting the cementitious matrix. Thaumasite can replace calcium silicate hydrates (C-S-H), leading to loss of strength and durability of materials containing GGBFS and LFS.

The hydration process of mixtures containing LFS and GGBFS is complex, involving multiple reactions that form calcium silicate hydrates (C-S-H), calcium aluminates, and calcium sulfoaluminates. The essential reactions influencing the formation of ettringite and thaumasite are (a) calcium hydroxide ($\text{Ca}(\text{OH})_2$) release: the hydration of LFS and GGBFS produces calcium hydroxide, raising the pH and facilitating ettringite and thaumasite formation; (b) alumina dissolution: the alumina in both LFS and GGBFS dissolves during hydration, contributing to the potential formation of ettringite; and (c) sulfate attack: the introduction of sulfates from external sources or impurities leads to the formation of ettringite and possibly thaumasite, especially in the presence of moisture and carbonates.

The formation of ettringite and thaumasite can have significant implications for the long-term performance of materials containing LFS and GGBFS, such as: (a) ettringite expansion: the expansion associated with delayed ettringite formation can cause cracking, reducing the durability of the material and (b) thaumasite deterioration: the conversion of C-S-H into thaumasite results in a loss of mechanical integrity, particularly in cold and moist environments, compromising the material's long-term strength.

Mitigating the formation of ettringite and thaumasite can be achieved by carbonating LFS and GGBFS using carbon dioxide and then adding polymerized elemental sulfur using bitumen. The mitigation mechanisms can be discussed in view of the role of carbonation of both LFS and GGBFS, as well as polymerized sulfur using bitumen. Carbonation involves reacting calcium hydroxide ($\text{Ca}(\text{OH})_2$) and other calcium-containing phases in LFS and GGBFS with carbon dioxide (CO_2) to form stable calcium carbonate (CaCO_3). This process reduces the availability of free calcium ions and hydroxides in the mixture, which are essential for forming ettringite and thaumasite. Carbonation lowers the system's pH by converting $\text{Ca}(\text{OH})_2$ into CaCO_3 . Ettringite formation is favored in highly alkaline environments, so reducing the pH through carbonation makes it less likely to form. Also, carbonating LFS and GGBFS binds calcium in a stable form as calcium carbonate, reducing the amount of free calcium needed for ettringite and thaumasite formation.

On the other hand, adding polymerized elemental sulfur using bitumen to the carbonated mixture can further mitigate the risks of ettringite and thaumasite formation. Elemental sulfur in its polymerized form can act as a binder, filling voids and providing additional resistance to moisture and sulfate attack, while bitumen acts as a protective matrix. Bitumen provides hydrophobic properties, limiting water ingress (i.e., as a moisture barrier). Moisture is a critical factor in forming ettringite and thaumasite, and reducing water exposure helps suppress these reactions. In addition, polymerized sulfur can stabilize sulfates, potentially preventing them from reacting with calcium and alumina in the mixture to form ettringite or thaumasite.

Therefore, the likelihood of ettringite formation is reduced by carbonating the mixture and reducing the free calcium hydroxide. Additionally, having polymerized sulfur in bitumen further helps by blocking moisture and sulfate movement, reducing the chances of delayed ettringite formation. Since thaumasite formation requires silicates, carbonates, and sulfates, the carbonation process binds calcium into stable carbonates, reducing free calcium and silicates available for thaumasite formation. Additionally, bitumen acts as a moisture barrier, mitigating the conditions for thaumasite to develop.

Moreover, carbonated LFS and GGBFS, combined with polymerized sulfur and bitumen, could improve the material's mechanical properties, providing additional strength and resistance to environmental degradation. Also, sequestering CO_2 would contribute to

carbon capture efforts while simultaneously using waste materials (LFS and GGBFS) and sulfur byproducts.

In another study by El-Sawy et al. [36], four compositions were used to prepare the PSC as: (i) Portland cement concrete (PCC) prepared by mixing 6.5 kg sand retained on a 0.3 mesh, 3.25 kg Portland cement, and 1.625 kg water; (ii) sulfate-resistance cement concrete (SRC) prepared by mixing 6.5 kg sand retained on a 0.3 mesh, 3.25 kg sulfate-resistant cement, and 1.625 kg water; (iii) PSC-ENB prepared using polymerized sulfur with 5-ethylidene-2-norbornene (ENB) 2% as the binder, fly ash, and dune sand with a composition ratio of polymerized sulfur (28%), fly ash (14%), and dune sand (58%); and (iv) PSC-Bitumen prepared using 2.5% bitumen as the binder, carbonated fly ash, and dune sand with composition ratio of polymerized sulfur (34.4%), carbonated fly ash (36.4%), and dune sand (28.9%). These samples were immersed for 24 months in a real-time sewerage sludge with pH 6.77–7.05, temperature 21–37 °C, turbidity 93–219 NTU, total dissolved solids 312–500 mg/L, electrical conductivity 708–998 $\mu\text{S}/\text{cm}^3$, sulfate 119–240 mg/L, nitrate 0.95–3.47 mg/L, chloride 79.3–187 mg/L, and bacteria count 12–163 $\times 10^6$ Cfu/100 mL.

Figure 15 displays the weight loss of the four tested compositions (PCC, SRC, PSC-ENB, and PSC-Bitumen) for up to 24 months. The PSC specimens revealed the most minor weight change, less than 2% in the case of PSC-ENB and less than 1% in the case of PSC-Bitumen. PCC and SRC, on the contrary, showed significant deterioration, losing up to 6 and 11% from their weights, respectively, within 24 months. The decreased weight depends on the resistance of the binding material to the acidic attack.

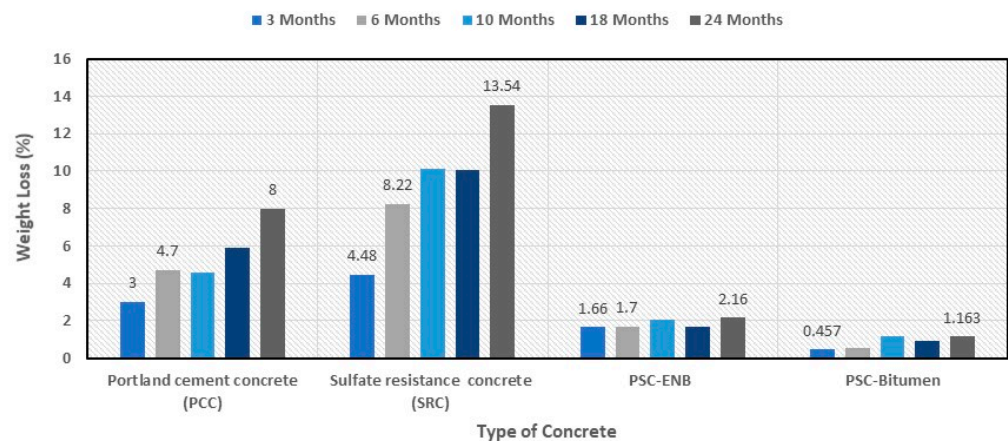


Figure 15. Weight loss of different concretes after 24 months of exposure to the harsh sewerage environment.

Figure 16 shows the compressive strength variations of the four different compositions (PCC, SRC, PSC-ENB, and PSC-Bitumen) after 24 months of exposure to the harsh sewerage environment. Significant reductions in compressive strength were observed for the PCC and SRC compared to PSC-Bitumen and PSC-ENB. This can be explained as Portland cement is mainly composed of four main minerals: tricalcium silicate [$3\text{CaO}\cdot\text{SiO}_2$], dicalcium silicate [$2\text{CaO}\cdot\text{SiO}_2$], tricalcium aluminate [$3\text{CaO}\cdot\text{Al}_2\text{O}_3$], and tetra-calcium Ferro aluminate [$4\text{CaO}\cdot\text{Fe}_2\text{O}_3\cdot\text{Al}_2\text{O}_3$]. These mineral products react with water to form several hydrated products, including high amounts of calcium hydroxide [$\text{Ca}(\text{OH})_2$] (Mohamed and Antia, 1998). Sulfate ions react with the hydration products of cement or cementitious material in two main forms [37]. One common source of sulfate attack on concrete is the reaction of sulfate ions with calcium hydroxide, which forms calcium sulfate [$\text{CaSO}_4\cdot 2\text{H}_2\text{O}$] (gypsum). Gypsum formation decreases the concrete's pH, and this causes softening of the concrete and loss of strength and mass [37,38]. In the presence of calcium hydroxide, sulfate ions react with tricalcium aluminate [$3\text{CaO}\cdot\text{Al}_2\text{O}_3\cdot(\text{C}_3\text{A})$] and convert them into ettringite [$6\text{CaO}\cdot\text{Al}_2\text{O}_3\cdot 3\text{SO}_4\cdot 32\text{H}_2\text{O}$] and mono-sulfo-aluminate. Ettringite formation also causes expansion and loss of concrete strength [39,40].

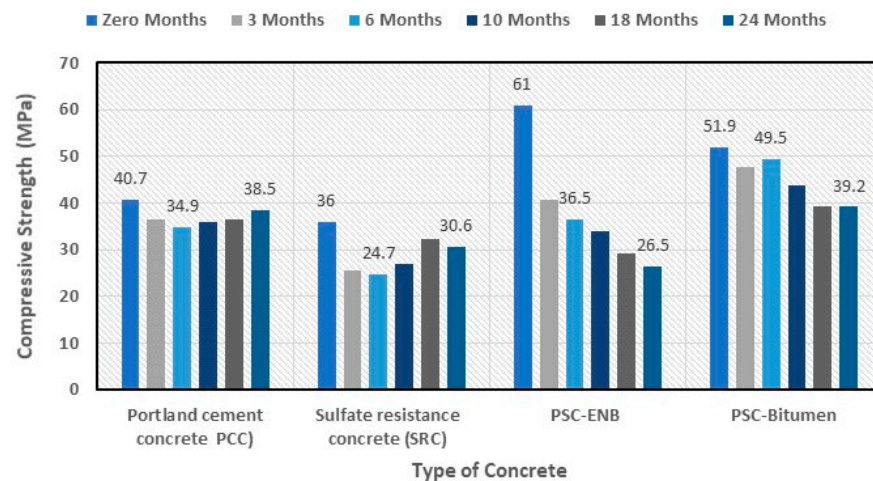


Figure 16. Compressive strength variations of different concretes after 24 months of exposure to the harsh sewerage environment.

Figure 17 shows the permeability variations of the four different compositions (PCC, SRC, PSC-ENB, and PSC-Bitumen) after 24 months of exposure to the harsh sewerage environment. The results indicated that the order of concretes with low permeability is PSC-Bitumen > PSC-ENB > PCC > SRC. To explain such results, one must realize that the polymerized sulfur prevented water penetration because it is hydrophobic. Also, most of the matrix comprises polymerized sulfur-coated aggregates and accumulated polymerized sulfur in the voids between particles. This, in turn, will lead to PSC having impermeable characteristics. Interestingly, some researchers [41] have found that the pore spaces of PSC, PCC, and SRC have approximately the same volume. However, the pores in the PSC are not connected, providing low permeability characteristics, while the pores of PCC concrete are connected. It is also noted that the permeability is highly dependent on the size of pore spaces, degree of connectivity between pores, grain shape, degree of packing, and cementation [42]. The reduced permeability should contribute to improved long-term durability and resistance to various forms of deterioration.

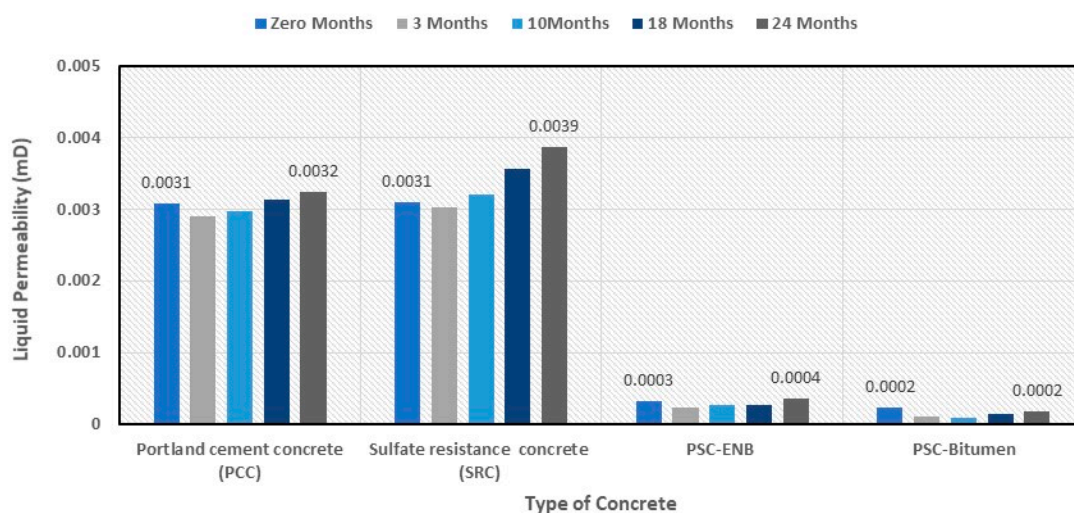


Figure 17. Variations in the permeabilities of different concretes after 24 months of exposure to the harsh sewerage environment.

In recent years, 3D printing has gained acceptance for its large-scale automated construction capabilities in the housing and infrastructure sectors [43]. It offers noteworthy advantages such as reducing the construction time and amount of generated wastes and

economic benefits by reducing the costs associated with traditional construction methods [44,45]. In extrusion-based 3D printing technology, PSC ingredients are selected, mixture design proportions are optimized, and 3D printing process parameters are optimized [46]. Moreover, techniques for including fiber reinforcement in 3D-printed structures have recently been developed [47–50].

In a study by Giwa et al. [43], the 3D-printed elemental sulfur concrete (ESC) samples, made from 50% elemental sulfur (not polymerized) and 50% natural sand, were placed inside a vacuum chamber (an ultimate vacuum pressure of 0.05 torr ($=3.248 \times 10^{-4}$ kPa)) at the ambient temperature (20 ± 5 °C) or an elevated temperature (55 ± 5 °C) and both the weight loss and flexural strength of the ESC samples were measured after three and seven days of exposure. The vacuum was imposed to simulate the extraterrestrial conditions for building on Mars. However, its relevance to the current study can be viewed by simulating an extreme condition during the discharging of hydrogen gas from the rock cavern, where the external pressure on the cavern would be higher than the pressure inside, hence creating tensile stresses in the cavern's structural system (i.e., sulfur concrete and the lining material). It is to be noted that, as per Caglayan et al. [51], the cavern's fluid pressure does not exceed 24% of the overburden pressure during hydrogen production and 80% during hydrogen injection (Figure 18). Thus, the cavern's fluid pressure is a function of the overburdened rock density and depth of the roof and the bottom of the cavern.

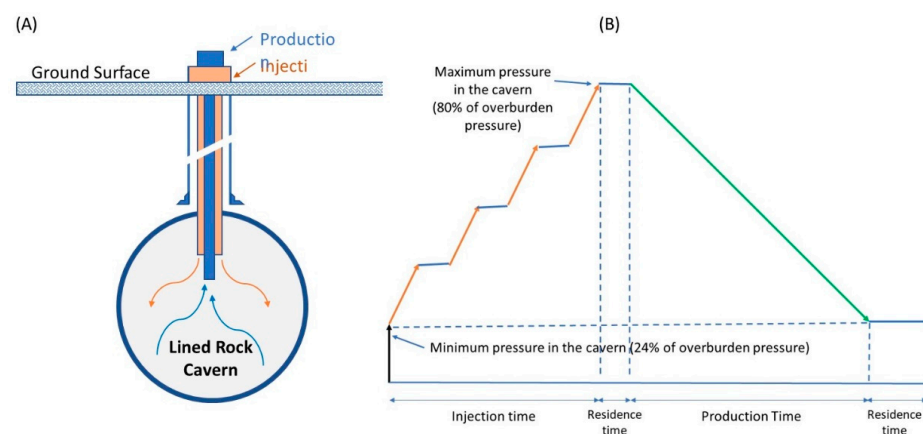


Figure 18. Schematic representation of (A) the lined rock cavern with the injection and production wells and (B) the stresses in the rock cavern during injection and production.

The results (Figure 19; data from Giwa et al. [43]) showed that: (i) at 20 °C, a negligible weight loss of 0.010% and 0.016% was measured after 3 and 7 days of exposure, respectively; (ii) when temperature was elevated to 55 °C and in the presence of vacuum, the weight loss significantly increased by an order of magnitude (from 0.82 and 0.92% at 3 and 7 days, respectively); (iii) as curing time increases from 3 to 7 days, an average of 66% increase in weight loss was measured, which is consistent with a study by Tucker [52], (who showed that when elemental sulfur was heated from 24–26 °C to 40–45 °C, the rate of sulfur sublimation increased by 80%, and with another study by Bradley (1951), who studied the rate of evaporation of rhombic sulfur at 15 °C–33 °C under different vacuum pressures and showed that an increase in the temperature significantly increases the vapor pressure of the rhombic sulfur crystals. Similar results were reported by Giwa et al. [43], who presented scanning electron microscopy images with voids due to vacuum exposure and sulfur vaporization; (iv) when compared to the control specimen printed and stored at ambient conditions, the flexural strength values decreased by 10.52% and 8.38% after 3 and 7 days due to the increase in porosity as voids are created in the microstructure of the printed sulfur concrete due to sulfur sublimation; and (v) since the decrease after 7 days (8.38%) was less than that after 3 days (10.52%), one could conclude that the curing time does not have an effect of the flexural strength development, which is consistent with a study by Nash and Moses [53], who showed no increase in the sublimation rate of frozen

sulfur melt (in the polymeric form), measured at 28 °C and 50 °C in 0.01 torr vacuum pressure, after 8 days. Therefore, the 3D-casted ESC possessed higher flexural strength than the conventional OPC concrete (3–5 MPa; at standard conditions), even after exposure to extreme vacuum and temperature conditions.

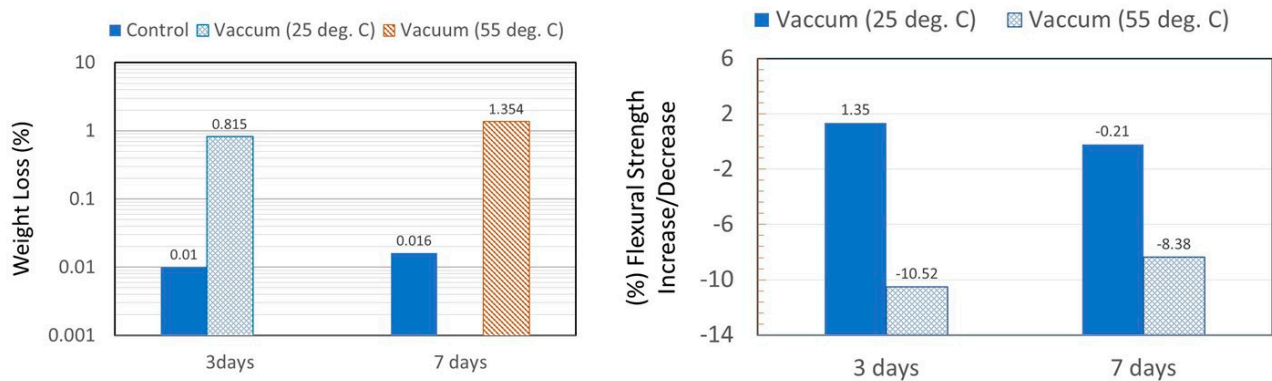


Figure 19. Physico-mechanical properties of 3D-printed elemental sulfur concrete (ESC) with a vacuum pressure of 0.05 torr and variable temperatures.

7. Discussion

The question that poses itself is how the PSC mixture components constitute a viable solution to storing hydrogen in lined rock caverns, or in other words, what is the role of each element in mitigating the formation of hydrogen sulfide and retarding the hydrogen diffusion through the PSC barrier? Using carbonated alkaline solid wastes, such as LFS and GGBFS, to inhibit the reaction between hydrogen and polymerized sulfur presents a feasible strategy for minimizing H_2S formation and improving the safety and reliability of hydrogen storage in bitumen–sulfur matrices. The role of each component is highlighted as follows. LFS can act as a barrier to hydrogen diffusion and act as a sulfur stabilizing agent. By acting as fillers in the bitumen–sulfur matrix, LFS can retard hydrogen diffusion due to increasing the density of the material and reducing the permeability of hydrogen, hence blocking hydrogen diffusion and minimizing the chances of the hydrogen–sulfur reaction. Stabilization of sulfur can be achieved due to the interaction of the silica and alumina content with sulfur to create a more stable structure, reducing sulfur’s reactivity with hydrogen.

Similarly, GGBFS has been shown to improve the impermeability of materials by increasing their density. When mixed with bitumen-based sulfur, GGBFS can fill the pores and voids, potentially creating a barrier to hydrogen diffusion. In addition, GGBFS can chemically stabilize the sulfur within the matrix, as the calcium content in the slag could bind with sulfur, reducing its reactivity with hydrogen and mitigating the risk of hydrogen sulfide (H_2S) formation.

When combined, LFS and GGBFS could have a synergistic effect on the bitumen-based sulfur matrix by enhancing its structural properties and minimizing hydrogen permeability. These materials are already known to improve the mechanical strength, durability, and chemical resistance of composite materials like concrete, and they could similarly enhance the bitumen–sulfur system of hydrogen storage.

The potential challenges to using carbonated alkaline wastes as aggregates with polymerized sulfur to form PSC include: (a) Homogeneous mixing: Ensuring a uniform distribution of LFS and GGBFS in the bitumen–sulfur matrix is crucial for achieving the desired barrier properties. Poor mixing could result in localized reactions or permeability variations; (b) Long-term durability: While these materials are known to improve the durability of construction materials, their long-term performance in a hydrogen storage environment, especially under high pressures and fluctuating temperatures, would need further studies; and (c) Hydrogen diffusion rates: While LFS and GGBFS could reduce hydrogen diffusion, the extent of their effectiveness in preventing hydrogen–sulfur reactions

would depend on factors like particle size distribution, matrix porosity, and interaction with bitumen.

Therefore, adding LFS and GGBFS to a bitumen-based polymerized sulfur matrix can be a promising approach to inhibiting hydrogen–sulfur reactions and minimizing hydrogen sulfide (H₂S) formation. These materials will likely enhance the matrix's structural integrity, impermeability, and chemical stability, making hydrogen storage in underground manufactured rock caverns more feasible. However, further research would be required to assess their long-term performance, especially under hydrogen-rich, high-pressure environments.

8. Conclusions

The demand for hydrogen is expected to grow significantly in the coming years, driven by its potential use in various sectors such as transportation, power generation, and heating. As the world approaches decarbonization, hydrogen is expected to be critical in transitioning to a clean energy future.

Hydrogen storage is a critical issue that needs to be addressed before widespread adoption of hydrogen fuel cells can occur. The geological storage methods for hydrogen storage are still in the early stages of development, and there is ongoing research and testing to address some of the limitations and challenges associated with each method. Ultimately, the choice of which geological reservoir to use for hydrogen storage will depend on the local geology, the amount of hydrogen to be stored, and the application's specific needs. Hydrogen can interact with geological formations through various chemical reactions, forming different compounds and minerals. Understanding these chemical interactions is crucial for multiple geological processes, including natural gas exploration, carbon sequestration, and geothermal energy production. Further research is needed to fully understand the complex chemical interactions between hydrogen and geological formations and their implications for various environmental and energy-related applications.

Storing hydrogen in a manufactured rock cavern is a viable technology requiring more research and development. Alternative composite materials to the currently used ones (i.e., ordinary Portland cement (OPC) concrete) are needed to mitigate the global warming potential and to have materials that are corrosion and fire resistant and have enough ductility to respond to the changes the underground conditions during the cyclic stress-deformation changes during the injection and withdrawal of hydrogen. Polymerized sulfur concrete (PSC) is a viable material that can replace OPC concrete.

The results showed that the manufactured PSC exhibited excellent physicochemical properties in terms of compressive strength (35–58 MPa), density (2.277–2.488 g/cm³), setting time (30–60 min), curing time (24 h), air content (4–8%), moisture absorption potential (0.17–0.3%), maximum volumetric shrinkage (1.69–2.0%), and max. service temperature (85–90 °C). Moreover, the PSC is nonconductive and classified with zero flame spread classification and fuel contribution. In addition, the SPC was found to be durable in harsh environmental conditions involving pressure, humidity, and pH variations. It is also capable of resisting corrosive environments.

In addition, the statistical modeling indicates that the overall mixture proportions of 32.5 wt.% polymerized sulfur, 32.5 wt.% dune sands, 17.5 wt.% LFS, and 17.5 wt.% GGBFS appear optimal for density values ranging from 2.43 to 2.44 g/cm³ and compressive strength ranging from 52.0 to 53.2 MPa, indicating that the PSC can sustain formation pressure up to about 5.3 km below the ground surface.

Therefore, by addressing the critical limitations of traditional materials, PSC proves to be a durable, environmentally sustainable solution for lined rock caverns, reducing the risk of hydrogen leakage and ensuring the integrity of storage systems. However, more research is required to enhance the PSC ductility and develop underground hydrogen storage field application guidelines.

Author Contributions: Conceptualization, A.-M.O.M.; methodology, A.-M.O.M. and M.E.G.; formal analysis, A.-M.O.M. and M.E.G.; writing—original draft, A.-M.O.M. and M.E.G.; writing—review

& editing, A.-M.O.M. and M.E.G. All authors have read and agreed to the published version of the manuscript.

Funding: This research received no external funding.

Institutional Review Board Statement: Not applicable.

Informed Consent Statement: Not applicable.

Data Availability Statement: The original contributions presented in the study are included in the article, further inquiries can be directed to the corresponding author.

Conflicts of Interest: Author Abdel-Mohsen O. Mohamed was a Chief Technology Advisor to Uberbinder Limited and declares that the research was conducted in the absence of any commercial or financial relationships that could be construed as a potential conflict of interest. The remaining authors declare that the research was conducted in the absence of any commercial or financial relationships that could be construed as a potential conflict of interest.

Appendix A. Technical Issues with Conventional Underground Storage Systems

The geological site design characteristics of the conventional storage methods are different (Table A1; data from Lord et al. [25] and Parks [54]):

- (i) The formation pressure is highly dependent on the depth of the storage reservoir;
- (ii) The formation temperature is about 14 MPa; the temperature ranges between about 40 and 42 °C;
- (iii) The Void volume is about $677 \times 10^3 \text{ m}^3$ for depleted hydrocarbon fields and aquifers, but it is higher ($580 \times 10^3 \text{ m}^3$) for salt and hard rock caverns;
- (iv) The well depth about 1.4 km for depleted hydrocarbon fields and aquifers, but it is lower (1.16 km) for salt and hard rock caverns;
- (v) Working gas: the actual storage capacity that can be repeatedly charged and discharged [54]; is 1912 tons of H₂, which is the same for all storage systems;
- (vi) Cushion gas, the base gas, is the amount of gas that stays permanently in the underground storage reservoir; it mostly gets trapped inside the geological structure and is used to keep the pressure at an adequate level for a gas delivery [55,56]; of 50 vol.% for depleted hydrocarbon fields and aquifer but it is lower (30 vol.%) for salt and hard rock caverns;
- (vii) A cushion gas of 956 tons of H₂ for depleted hydrocarbon fields and aquifers, but it is lower (574 tons of H₂) for salt and hard rock caverns; and
- (viii) The total hydrogen storage is 2868 tons of H₂ for depleted hydrocarbon fields and aquifers, but it is lower (2486 tons of H₂) for salt and hard rock caverns.

Table A1. Detailed information on geologic site design characteristics.

Geologic Storage Site Design Characteristics (Units)	Storage Methods			
	Conventional			Unconventional
	Depleted Hydrocarbon Fields	Aquifer	Salt Caverns	Hard Rock Caverns
Formation pressure (MPa)	13.76	13.76	13.79	13.79
Formation temperature (°C)	42.1	42.1	37.9	37.9
Void volume (m ³)	676,941	676,941	580,000	580,000
Well depth (m)	1403	1403	1158	1158
Working gas (tons H ₂)	1912	1912	1912	1912
Cushion gas percent of total volume (%)	50	50	30	30
Cushion gas (tons H ₂)	956	956	574	574
Total H ₂ stored on site (tons H ₂)	2868	2868	2486	2486

Each hydrogen storage method has advantages and disadvantages, and the most suitable method depends on the specific application and requirements (Table A2). More research is needed to improve the efficiency and practicality of each storage method and to develop new storage methods that can meet the needs of a wide range of applications.

Table A2. Conventional hydrogen storage methods in geological reservoirs.

Storage Method	Advantages	Disadvantages
Depleted oil and gas fields	<ul style="list-style-type: none"> Proven track record of storing hydrocarbons safely and effectively Existing infrastructure can be repurposed for hydrogen storage High storage capacity and potential for large-scale storage 	<ul style="list-style-type: none"> Potential risk of hydrogen leakage into the environment High cost of retrofitting existing infrastructure for hydrogen storage
Aquifers	<ul style="list-style-type: none"> Abundance of potential storage sites Potential for large-scale storage Low cost compared to other options 	<ul style="list-style-type: none"> Limited knowledge of the long-term stability of aquifers for hydrogen storage Risk of contamination of water resources
Salt caverns	<ul style="list-style-type: none"> Large storage capacity and potential for large-scale storage Ability to store gas at high pressures Potential for cost-effective storage solutions 	<ul style="list-style-type: none"> High initial capital investment for cavern creation and equipment Potential leakage, which can lead to contaminated groundwater if not properly managed Risk of cavern collapse due to geological instability or human error during the creation or maintenance of the caverns.

However, since hydrogen plays a vital role in various geological processes, it can interact with geological formations through a variety of chemical reactions, such as hydration, dissolution, and redox [42]. Hydrating rocks can lead to the formation of new minerals, such as clays, and weaken the rock structure over time. Dissolution can lead to the release of elements into solution and cause changes in the rock structure over time. The redox reactions can lead to hydrogen sulfide (H₂S) formation that modifies the redox potential and the pH of pore waters [57,58], triggering further fluid–rock reactions. H₂S can also compromise the infrastructure due to its corrosive, flammable, and toxic nature [59]. Moreover, such reactions could also lead to some deterioration in the caprock porosity and permeability, presenting a better seal and preventing leakage [60,61] or creating new leakage paths [62]. In addition, there are still some technical challenges that need to be overcome, such as:

- (1) Geological Characteristics: Finding suitable reservoirs that can store hydrogen safely and efficiently requires identifying geological formations that can contain hydrogen without leaking or causing environmental damage. Previous studies have indicated that suitable reservoirs for hydrogen storage must have specific geological characteristics, such as high porosity (to provide the storage capacity) and permeability (to ensure injectivity of the fluids), low levels of natural gas or other impurities, and stable rock formations that can withstand the high pressures associated with hydrogen storage [7,9,63]. (Ref. [7]; Carneiro et al., 2019 [9]). To address this challenge, it is essential to conduct detailed geological surveys and assessments to identify suitable hydrogen storage sites and develop advanced imaging and monitoring technologies to detect and prevent leaks and other environmental risks.
- (2) Geological Complexity: Geological formations can be highly variable and heterogeneous, with variations in permeability, porosity, and mineralogy. This can make it difficult to predict the behavior of hydrogen in the reservoir and to design storage facilities optimized for the site's specific conditions. For example, studies conducted

- by Matosa et al. [7] and Carneiro et al. [63] found that the performance of underground hydrogen storage facilities can be affected by faults and fractures in the reservoir rock.
- (3) **Geological Compatibility:** Not all geological formations are suitable for hydrogen storage, and those that are suitable may require additional treatment or modification to ensure safe and efficient hydrogen storage. For example, some reservoirs may contain impurities or contaminants that can react with hydrogen or reduce storage capacity, while others may require modification to improve their porosity and permeability [63].
 - (4) **Reservoir Integrity:** Geological reservoirs are not static, and their properties can change over time due to factors such as tectonic activity, subsidence, chemical interactions, and fluid flow. These changes can affect the performance of hydrogen storage facilities, and ongoing monitoring and maintenance are necessary to ensure the integrity of the reservoirs [63].
 - (5) **Leakage Potential:** Hydrogen has a small molecular size, which can make it difficult to contain and can lead to leakage through imperfections in storage infrastructure, such as wells or seals [10,51,63]. Moreover, hydrogen is highly flammable and can pose safety risks if it leaks into the atmosphere.
 - (6) **Well Integrity:** Over time, wells can degrade due to exposure to corrosive fluids and thermal and mechanical stress [64]. This can lead to leaks and pose safety risks.
 - (7) **Injection and Withdrawal Rates:** The injection and withdrawal rates of hydrogen from geological reservoirs can be limited by the properties of the reservoir rock and the design of the storage facility [65–67]. The permeability of the reservoir rock can affect the rate at which hydrogen can be injected or withdrawn. Also, the injection and withdrawal wells' design can affect the storage facility's efficiency, and the injection and withdrawal rates of hydrogen can be limited by the size and connectivity of the pore space in the reservoir rock.
 - (8) **Seismic and Geo-mechanical Stability:** The injection and withdrawal of hydrogen can induce changes in the subsurface pressure and stress state, potentially leading to seismic activity or geo-mechanical deformation. Moreover, the long-term storage of hydrogen can also lead to reservoir compaction or expansion, which can affect the stability of the storage formation.
 - (9) **Hydrogen Purity:** The purity of hydrogen stored in geological reservoirs can be affected by various factors, including the composition of the reservoir fluids, impurities in the injected hydrogen, and the potential for chemical reactions between the hydrogen and the reservoir rock. Impurities such as carbon dioxide, methane, and hydrogen sulfide can reduce stored hydrogen's energy content and quality, making it less valuable.
 - (10) **Hydrogen Storage Techniques:** The choice of hydrogen storage technique can also affect the technical challenges associated with hydrogen storage in geological reservoirs. For example, hydrogen storage in gas must be compressed to high pressures to achieve adequate storage densities. This can increase the energy requirements and costs associated with storage. On the other hand, if hydrogen is stored as a solid or liquid, it can reduce the energy requirements and increase the storage density. Still, it may require specialized storage facilities and handling procedures.
 - (11) **Reservoir Monitoring:** Once a reservoir has been selected for hydrogen storage, monitoring it to ensure its stability and integrity over time is necessary. This can be challenging, as hydrogen can diffuse into the surrounding rock formations, potentially reducing the overall storage capacity of the reservoir.
 - (12) **Safety Risks:** Hydrogen is highly flammable and explosive, and storing and transporting large quantities of hydrogen can pose significant safety risks to workers and the general public. The risk of hydrogen releases from storage facilities can be substantial, particularly in a well failure or equipment malfunction.

References

1. Statista Research Department. Hydrogen Demand Worldwide from 2019 to 2021, with a Forecast for 2030. 2024. Available online: <https://www.statista.com/statistics/1121206/global-hydrogen-demand/> (accessed on 1 September 2024).
2. IEA. The Future of Hydrogen: Seizing Today's Opportunities. Available online: <https://www.iea.org/reports/the-future-of-hydrogen> (accessed on 15 August 2024).
3. Ravn Nielsen, E.; Prag, C.B. Learning Points from Demonstration of 1000 Fuel Cell Based Micro-CHP units—Summary of Analyses from the Ene.Field Project. 2017. Available online: <http://enefield.eu/wpcontent/uploads/2017/10/ene.field-Summary-Report.pdf> (accessed on 15 August 2024).
4. Nagashima, M. *Japan's Hydrogen Strategy and Its Economic and Geopolitical Implications*; IFRI Centre for Energy: Paris, France, 2018. Available online: www.ifri.org/en/publications/etudes-de-lifri/japans-hydrogen-strategyand-its-economic-and-geopolitical-implications (accessed on 10 July 2024).
5. IEA. *The Future of Petrochemicals: Towards More Sustainable Plastics and Fertilisers*; IEA: Paris, France, 2018.
6. HYBRIT. HYBRIT—Towards Fossil-Free Steel. 2019. Available online: www.hybritdevelopment.com/ (accessed on 10 July 2024).
7. Matosa, C.R.; Carneiro, J.F.; Silva, P.P. Overview of largescale underground energy storage technologies for integration of renewable energies and criteria for reservoir identification. *J. Energy Storage* **2019**, *21*, 241–258. [CrossRef]
8. Tarkowski, R. Underground hydrogen storage: Characteristics and prospects. *Renew. Sustain. Energy Rev.* **2019**, *105*, 86–94. [CrossRef]
9. Zivar, D.; Kumar, S.; Foroozesh, J. Underground hydrogen storage: A comprehensive review. *Int. J. Hydrogen Energy* **2020**, *46*, 23436–23462. [CrossRef]
10. Cihlar, J.; Mavins, D.; Van Der Leun, K. *Picturing the Value of Underground Gas Storage to the European Hydrogen System*; Guidehouse: Chicago, IL, USA, 2021.
11. Elberry, A.M.; Thakur, J.; Santasalo-Aarnio, A.; Larmi, M. Large-scale compressed hydrogen storage as part of renewable electricity storage systems. *Int. J. Hydrog. Energy* **2021**, *46*, 15671–15690. [CrossRef]
12. Kruck, O.; Crotagino, F.; Prelicz, R.; Rudolph, T. *Overview on All Known Underground Storage Technologies for Hydrogen*; HyUnder: Huesca, Spain, 2013.
13. HyUnder. Assessment of the Potential, the Actors and Relevant Business Cases for Large Scale and Long-Term Storage of Renewable Electricity by Hydrogen Underground Storage in Europe (Executive Summary). 2014. Available online: http://hyunder.eu/wp-content/uploads/2016/01/D8.1_HyUnder-Executive-Summary.pdf (accessed on 10 July 2024).
14. Bauer, S.; Beyer, C.; Dethlefsen, F.; Dietrich, P.; Duttmann, R.; Ebert, M.; Feeser, V.; Görke, U.; Köber, R.; Kolditz, O.; et al. Impacts of the use of the geological sub-surface for energy storage: An investigation concept. *Environ. Earth Sci.* **2013**, *70*, 3935–3943. Available online: <https://link.springer.com/article/10.1007/s12665-013-2883-0> (accessed on 1 July 2024). [CrossRef]
15. Carnot-Gandolphe, S. *Underground Gas Storage & LNG storage market in the World 2015–2035*, 6th ed.; CEDIGAS. Available online: <https://www.cedigaz.org/> (accessed on 1 July 2024).
16. Lemieux, A.; Sharp, K.; Shkarupin, A. Preliminary assessment of underground hydrogen storage sites in Ontario, Canada. *Int. J. Hydrogen Energy* **2019**, *44*, 15193–15204. [CrossRef]
17. Sofregaz US Inc.; Song, J.; Zhang, D. *Commercial Potential of Natural Gas Storage in Lined Rock Caverns*; Sofregaz US Inc.: Seattle, WA, USA, 1999; 200 LRC; p. 141.
18. Miocic, J.; Heinemann, N.; Edlmann, K.; Scafidi, J.; Molaei, F.; Alcalde, J. Underground hydrogen storage: A review. In *Enabling Secure Subsurface Storage in Future Energy Systems*; Geological Society, Miocic, J.M., Heinemann, N., Edlmann, K., Alcalde, J., Schultz, R.A., Eds.; Special Publications: London, UK, 2023; Volume 528, pp. 73–86. [CrossRef]
19. Kumar, K.R.; Makhmutov, A.; Spiers, C.J.; Hajibeygi, H. Geomechanical simulation of energy storage in salt formations. *Sci. Rep.* **2021**, *11*, 19640. [CrossRef]
20. Spiers, C.J.; Schutjens, P.M.T.M.; Brzesowsky, R.H.; Peach, C.J.; Liezenberg, J.L.; Zwart, H.J. Experimental determination of constitutive parameters governing creep of rocksalt by pressure solution. *Geol. Soc. Lond. Spec. Publ.* **1990**, *54*, 215–227. [CrossRef]
21. Asgari, A.; Ramezanzadeh, A.; Jalali, S.M.E.; Brouard, B. Stability analysis of salt cavern gas storage using 2D thermo-hydro-mechanical finite-element software. *J. Min. Environ.* **2020**, *11*, 77–97. [CrossRef]
22. Urai, J.L.; Schmatz, J.; Klaver, J. Over-Pressured Salt Solution Mining Caverns and Leakage Mechanisms—Phase 1: Micro-Scale Processes, Project KEM-17. MaP—Microstructure and Pores GmbH: Aachen, Germany, 2019.
23. Hunsche, U.; Hampel, A. Rock salt—The mechanical properties of the host rock material for a radioactive waste repository. *Eng. Geol.* **1999**, *52*, 271–291. [CrossRef]
24. Leister, N.; Yfantis, G.; Murray, E.; McNroy, D.; Kopan, Y. *Salt Cavern Appraisal for Hydrogen and Gas Storage; Stage 2*; ETI: Sunrise, FL, USA; Atkins: Epsom, UK, 2018.
25. Lord, A.S.; Kobos, P.H.; Borns, D.J. Geologic storage of hydrogen: Scaling up to meet city transportation demands. *Int. J. Hydrogen Energy* **2014**, *39*, 15570–15582. [CrossRef]
26. Glamheden, R.; Curtis, P. Excavation of a cavern for high-pressure storage of natural gas. *Tunn. Undergr. Sp. Technol.* **2006**, *21*, 56–67. [CrossRef]
27. Mohamed, A.M.O.; El Gamal, M. *Sulfur Concrete for the Construction Industry: A Sustainable Development Approach*; J. Ross Publishing: New York, NY, USA, 2010.

28. Kyuhun, K. Mechanical Properties of Sulfur Concrete. Master's Thesis, Urban Infrastructure Engineering Program, Graduate School of Ulsan National Institute of Science and Technology (UNIST), Ulsan, Republic of Korea, 2013.
29. Mohamed, A.M.O.; Boily, J.F.; Hossein, M.; Hassani, F.P. Ettringite Formation in Lime-Remediated Mine Tailings: I. Thermodynamic Modelling. *Can. Inst. Min. Metall. Pet. (CIM) Bull.* **1995**, *88*, 69–75.
30. Moon, J.; Kalb, P.D.; Milian, L.; Northrup, P.A. Characterization of a sustainable sulfur polymer concrete using activated fillers. *Cem. Concr. Compos.* **2016**, *67*, 20–29. [[CrossRef](#)]
31. El Gamal, M.M.; El-Dieb, A.S.; Mohamed, A.M.O.; El Sawy, K.M. Performance of modified sulfur concrete exposed to actual sewerage environment with variable temperature, humidity and gases. *J. Build. Eng.* **2017**, *11*, 1–8. [[CrossRef](#)]
32. Mohamed, A.M.O.; El Gamal, M.; Hameedi, S. *Sustainable Utilization of Carbon Dioxide in Waste Management*; Elsevier: Amsterdam, The Netherlands, 2022; ISBN 9780128234181. 606p.
33. Al-Raqeb, H.; Ghaffar, S.H.; Al-Kheetan, M.J.; Chougan, M. Understanding the challenges of construction demolition waste management towards circular construction: Kuwait Stakeholder's perspective. *Clean. Waste Syst.* **2023**, *4*, 100075, ISSN 2772-9125. [[CrossRef](#)]
34. ACI Committee 548. *Guide for Mixing and Placing Sulfur Concrete in Construction*; ACI: Farmington Hills, MI, USA, 1993.
35. El Gamal, M.; El-Sawy, K.; Mohamed, A.M.O. Integrated Mixing Machine for Sulfur Concrete Production. *Case Stud. Constr. Mater. J.* **2021**, *14*, e00495. [[CrossRef](#)]
36. El-Sawy, K.; El Gamal, M.; El-Dieb, A.; Mohamed, A.M.O. Optimization of New Modified Sulfur Concrete For Sewer Applications. In Proceedings of the Fifth International Conference on Construction Materials Performance, Innovations, and Structural Implications, ConMat'15, Paper ID 138, Whistler, BC, Canada, 19–21 August 2015.
37. Attiogbe, E.K.; Rizkalla, S.H. Response of concrete to sulfuric acid attack. *ACI Mater J.* **1988**, *84*, 481–488.
38. Saricimen, H.; Shameem, M.; Barry, M.; Ibrahim, M.; Abbasi, T. Durability of proprietary cementitious materials for use in wastewater transport systems. *Cem. Concr. Compos.* **2003**, *25*, 421–427. [[CrossRef](#)]
39. Collepardi, M. Mechanism of deterioration and mix design of durable concrete structures. In Proceedings of the P.K. Mehta Symposium on Durability of Concrete, Nice, France, 23 May 1994; pp. 35–60.
40. Rasheduzzafar, F.H.D.; Al-Gahtani, A.S.; Al-Sadoun, S.S.; Bader, M.A. Influence of Cement Composition on the Corrosion of Reinforcement and Sulfate Resistance of Concrete. *ACI Mater J.* **1990**, *87*, 114–122.
41. Vroom, A.H. Sulfur Concrete Goes Global. *Concr. Int.* **1998**, *20*, 68–71.
42. Mohamed, A.M.O.; Paleologos, E.K. *Fundamentals of Geo-environmental Engineering: Understanding Soil, Water, and Pollutant Interaction and Transport*; eBook; Elsevier: Amsterdam, The Netherlands, 2018; ISBN 9780128051450. 708p.
43. Giwa, I.; Hebert, M.; Lamendola, J.; Fiske, M.; Kazemian, A. Planetary Robotic Construction Using Large-Scale 3D Printing with Sulfur Concrete. In Proceedings of the ASCE Construction Research Congress, Des Moines, Iowa, 20–23 March 2024; pp. 586–596.
44. Bos, F.; Wolfs, R.; Ahmed, Z.; Salet, T. Additive manufacturing of concrete in construction: Potentials and challenges of 3D concrete printing. *Virtual Phys. Prototyp.* **2016**, *11*, 209–225. [[CrossRef](#)]
45. Buswell, R.A.; De Silva, W.R.L.; Jones, S.Z.; Dirrenberger, J. 3D printing using concrete extrusion: A roadmap for research. *Cem. Concr. Res.* **2018**, *112*, 37–49. [[CrossRef](#)]
46. Perrot, A.; Rengeard, D.; Pierre, A. Structural built-up of cement-based materials used for 3D-printing extrusion techniques. *Mater. Struct.* **2016**, *49*, 1213–1220. [[CrossRef](#)]
47. Ye, J.; Cui, C.; Yu, J.; Yu, K.; Dong, F. Effect of polyethylene fiber content on workability and mechanical-anisotropic properties of 3D printed ultra-high ductile concrete. *Constr. Build. Mater.* **2021**, *281*, 122586. [[CrossRef](#)]
48. Kazemian, A.; Seylabi, E.; Ekenel, M. Concrete 3D Printing: Challenges and Opportunities for the Construction Industry. In *Innovation in Construction: A Practical Guide to Transforming the Construction Industry*; Springer: Cham, Switzerland, 2022; pp. 277–299.
49. Sun, X.; Zhou, J.; Wang, Q.; Shi, J.; Wang, H. PVA fibre reinforced high-strength cementitious composite for 3D printing: Mechanical properties and durability. *Addit. Manuf.* **2022**, *49*, 102500. [[CrossRef](#)]
50. Ahmed, H.; Giwa, I.; Game, D.; Arce, G.; Noorvand, H.; Hassan, M.; Kazemian, A. Automated Reinforcement during Large-Scale Additive Manufacturing: Structural Assessment of a Dual Approach. *Buildings* **2024**, *14*, 1167. [[CrossRef](#)]
51. Caglayan, D.G.; Weber, N.; Heinrichs, H.U.; Linßen, J.; Robinius, M.; Kukla, P.A.; Stolten, D. Technical potential of salt caverns for hydrogen storage in Europe. *Int. J. Hydrogen Energy* **2020**, *45*, 6793–6805. [[CrossRef](#)]
52. Tucker, R.P. Notes on the Sublimation of Sulfur between 25° and 50 °C. *Ind. & Eng. Chem.* **1929**, *21*, 44–47.
53. Nash, D.B.; Moses, J.I. Vacuum weathering of sulfur: Temperature effects and applications to Io. *Geophys. Res. Lett.* **1988**, *15*, 697–700. [[CrossRef](#)]
54. Parks, G.D. Chevron Phillips Hydrogen Cavern Clemens Terminal. 2007. Available online: https://www.internationalpipelineconference.com/presentation_Files/1030_PARKS-Clemens_Release-Final.ppt.zip (accessed on 5 June 2024).
55. Flanigan, O. Chapter 6—Characteristics of underground storage. In *Underground Gas Storage Facilities*; Flanigan, O., Ed.; Gulf Professional Publishing: Houston, TX, USA, 1995; pp. 54–67.
56. Stone, H.B.J.; Veldhuis, I.; Richardson, R.N. Underground hydrogen storage in the UK. *Geol. Soc. Lond. Spec. Publ.* **2009**, *313*, 217–226. [[CrossRef](#)]
57. Mazarei, M.; Davarpanah, A.; Ebadati, A.; Mirshekari, B. The feasibility analysis of underground gas storage during an integration of improved condensate recovery processes. *J. Pet. Explor. Prod. Technol.* **2018**, *9*, 397–408. [[CrossRef](#)]

58. Truche, L.; Jodin-Caumon, M.-C.; Lerouge, C.; Berger, G.; Mosser-Ruck, R.; Giffaut, E.; Michau, N. Sulphide mineral reactions in clay-rich rock induced by high hydrogen pressure. Application to disturbed or natural settings up to 250 °C and 30 bar. *Chem. Geol.* **2013**, *351*, 217–228. [[CrossRef](#)]
59. Wei, T.; Lim, K.; Tseng, Y.; Chan, S. A review on the characterization of hydrogen in hydrogen storage materials. *Renew. Sustain. Energy Rev.* **2017**, *79*, 1122–1133. [[CrossRef](#)]
60. Heinemann, N.; Alcalde, J.; Miocic, J.M.; Hangx, S.J.T.; Kallmeyer, J.; Ostertag-Henning, C.; Hassanpouryouzband, A.; Thaysen, E.M.; Strobel, G.J.; Schmidt-Hattenberger, C.; et al. Enabling large-scale hydrogen storage in porous media—The scientific challenges. *Energy Environ. Sci.* **2021**, *14*, 853–864. [[CrossRef](#)]
61. Bin Navaid, H.; Emadi, H.; Watson, M. A comprehensive literature review on the challenges associated with underground hydrogen storage. *Int. J. Hydrog. Energy* **2023**, *48*, 10603–10635. [[CrossRef](#)]
62. Kampman, N.; Busch, A.; Bertier, P.; Snippe, J.; Hangx, S.; Pipich, V.; Di, Z.; Rother, G.; Harrington, J.F.; Evans, J.P.; et al. Observational evidence confirms modelling of the long-term integrity of CO₂-reservoir cap rocks. *Nat. Commun.* **2016**, *7*, 12268. [[CrossRef](#)] [[PubMed](#)]
63. Carneiro, J.F.; Matosa, C.R.; van Gessel, S. Opportunities for large-scale energy storage in geological formations in mainland Portugal. *Renew. Sustain. Energy Rev.* **2019**, *99*, 201–211. [[CrossRef](#)]
64. Dhawan, S. 2023 Well Integrity-2023. Available online: <https://jpt.spe.org/well-integrity-2023> (accessed on 1 June 2024).
65. Feldmann, F.; Hagemann, B.; Ganzer, L.; Panfilov, M. Numerical simulation of hydrodynamic and gas mixing processes in underground hydrogen storages. *Environ. Earth Sci.* **2016**, *75*, 1165. [[CrossRef](#)]
66. Sainz-Garcia, A.; Abarca, E.; Rubi, V.; Grandia, F. Assessment of feasible strategies for seasonal underground hydrogen storage in a saline aquifer. *Int. J. Hydrog. Energy* **2017**, *42*, 16657e66. [[CrossRef](#)]
67. Pfeiffer, W.T.; Beyer, C.; Bauer, S. Hydrogen storage in a heterogeneous sandstone formation: Dimensioning and induced hydraulic effects. *Pet. Geosci.* **2017**, *23*, 315–326. [[CrossRef](#)]

Disclaimer/Publisher’s Note: The statements, opinions and data contained in all publications are solely those of the individual author(s) and contributor(s) and not of MDPI and/or the editor(s). MDPI and/or the editor(s) disclaim responsibility for any injury to people or property resulting from any ideas, methods, instructions or products referred to in the content.